Comparison of 20 exclusive reactions at large t

C. White,[4,*] R. Appel,[1,5,†] D. S. Barton,[1] G. Bunce,[1] A. S. Carroll,[1]
H. Courant,[4] G. Fang,[4,‡] S. Gushue,[1] K. J. Heller,[4] S. Heppelmann,[2]
K. Johns,[4,§] M. Kmit,[1,‖] D. I. Lowenstein,[1] X. Ma,[3] Y. I. Makdisi,[1]
M. L. Marshak,[4] J. J. Russell,[3]
and M. Shupe[4,§]

[1]*Brookhaven National Laboratory, Upton, New York 11973*
[2]*Pennsylvania State University, University Park, Pennsylvania 16802*
[3]*University of Massachusetts Dartmouth, N. Dartmouth, Massachusetts 02747*
[4]*University of Minnesota, Minneapolis, Minnesota 55455*
[5]*New York University, New York, New York 10003*

(Received 28 May 1993)

We report a study of 20 exclusive reactions measured at the AGS at 5.9 GeV/c incident momentum, 90° center of mass. This experiment confirms the strong quark flow dependence of two-body hadron-hadron scattering at large angle. At 9.9 GeV/c an upper limit had been set for the ratio of cross sections for $(\bar{p}p \to \bar{p}p)/(pp \to pp)$ at 90° c.m., with the ratio less than 4%. The present experiment was performed at lower energy to gain sensitivity, but was still within the fixed angle scaling region. A ratio $R(\bar{p}p/pp) \approx 1/40$ was measured at 5.9 GeV/c, 90° c.m. in comparison to a ratio near 1.7 for small angle scattering. In addition, many other reactions were measured, often for the first time at 90° c.m. in the scaling region, using beams of $\pi^{\pm}$, $K^{\pm}$, p, and $\bar{p}$ on a hydrogen target. There are similar large differences in cross sections for other reactions: $R(K^-p \to \pi^+\Sigma^-/K^-p \to \pi^-\Sigma^+) \approx 1/12$, for example. The relative magnitudes of the different cross sections are consistent with the dominance of quark interchange in these 90° reactions, and indicate that pure gluon exchange and quark-antiquark annihilation diagrams are much less important. The angular dependence of several elastic cross sections and the energy dependence at a fixed angle of many of the reactions are also presented.

PACS number(s): 13.75.−n, 13.85.Dz, 13.85.Fb

INTRODUCTION

Two-body to two-body exclusive scattering represents a very small fraction of scattering at high energy. It is much more likely that particles will fragment. Even more rare is exclusive scattering at large center-of-mass angles. For example, the total elastic cross section is about 1/4 of the total cross section for proton-proton scattering at 10 GeV/c incident momentum; the 90° elastic scattering cross section is less than a part per million of the 0° elastic cross section.

Despite its rarity, large angle exclusive scattering is of great interest because it allows us to glimpse short-distance interactions directly. The impact parameter decreases inversely with the momentum transferred in the interaction, p_T. This distance is given by $\hbar/p_T$. Even for a beam momentum of 5.9 GeV/c, this distance is much smaller than the radius of a proton, 0.1 fm compared to 0.9 fm.

We measured 20 two-body, wide-angle, exclusive reactions at 5.9 GeV/c incident momentum Ref. [1a]. These reactions, listed in Table I, were measured in the same apparatus. All the reactions of the same beam and spectrometer polarity were measured simultaneously. The BNL Alternate Gradient Synchrotron (AGS) experiment E838 followed E755, in which our group measured exclusive wide-angle hadronic interactions with an incident beam momentum of 9.9 GeV/c [1]. The beam momentum for E838 was reduced to 5.9 GeV/c, increasing the differential cross sections by factors of about 90 and 50 for baryon-baryon and meson-baryon elastic interactions, respectively, while remaining within the observed scaling region.

Both experiments (E755 and E838) had the goal to explore the dynamics of large angle scattering. Previously, the energy dependence of fixed angle elastic scattering and angular dependence had been measured, but a comprehensive study of two-body exclusives at large angle, including nonelastic reactions, had not been done. It had been observed that fixed angle elastic cross sections show scaling behavior, falling as a high power of energy, as opposed to the exponential fall-off observed for small angles. Scaling is seen for incident momenta $p > 5$ GeV/c for 90° scattering. It had also been observed that, for incident momenta above roughly 5 GeV/c, the angular dependence of the cross sections flattened in the region of 90° c.m. These observations indicate that large angle scattering for $Q^2 > 5$ (GeV/c)^2 has different dynamics from small angle scattering. Moreover, the observed power of the energy dependence agrees well with dimensional

*Current address: Ohio State University, Columbus, OH 43210.
†Current address: Yale University, New Haven, CT 06511.
‡Current address: Harvard University, Cambridge, MA 02139.
§Current address: University of Arizona, Tucson, AZ 85721.
‖Current address: Niels Bohr Institute, Copenhagen, Denmark.

TABLE I. Measured reactions presented in this paper. The reactions are written as (beam + target) → (spectrometer particle + side particle). Reactions 1, 2, 3, 17, and 18 were measured with either final-state particle in the spectrometer.

Meson-baryon reactions	
1	$\pi^+ p \to p\pi^+$
2	$\pi^- p \to p\pi^-$
3	$K^+ p \to pK^+$
4	$K^- p \to pK^-$
5	$\pi^+ p \to p\rho^+$
6	$\pi^- p \to p\rho^-$
7	$K^+ p \to pK^{*+}$
8	$K^- p \to pK^{*-}$
9	$K^- p \to \pi^- \Sigma^+$
10	$K^- p \to \pi^+ \Sigma^-$
11	$K^- p \to \Lambda\pi^0$
12	$\pi^- p \to \Lambda K^0$
13	$\pi^+ p \to \pi^+ \Delta^+$
14	$\pi^- p \to \pi^- \Delta^+$
15	$\pi^- p \to \pi^+ \Delta^-$
16	$K^+ p \to K^+ \Delta^+$
Baryon-baryon reactions	
17	$pp \to pp$
18	$\bar{p}p \to p\bar{p}$
19	$\bar{p}p \to \pi^+\pi^-$
20	$\bar{p}p \to K^+K^-$

counting arguments which imply that only the valence quarks participate in large angle exclusive scattering.

By comparing reactions with different combinations of valence quarks in the initial and final states, our experiments were conceived to investigate the quark flow dependence. For example, elastic processes can be mediated by exchanges of gluons and, if gluon exchange dominated these reactions, all elastic meson-baryon cross sections would be similar in magnitude. If, on the other hand, the dominant process involved the exchange of quarks between the interacting hadrons, elastic reactions where the interacting hadrons have no valence quarks in common would be suppressed. One would then expect the 90° $\bar{p}p$ and K^-p elastic cross sections to be much smaller than pp and K^+p, respectively. By including final states with new valence quarks, different from the initial states, we could also explore the importance of quark annihilation and creation for 90° scattering.

Both experiments (E755 and E838) scattered tagged beams of $\pi^\pm$, $K^\pm$, p, and $\bar{p}$ from hydrogen, and required an outgoing track at large angle near the kinematic limit in transverse momentum, as measured in a magnetic spectrometer. The scattered charged tracks on the opposite side were observed in a proportional chamber array. Missing mass, momentum conservation, and track topology were used to identify two-body exclusive reactions. The first experiment (E755)[1] measured cross sections or set upper limits for 14 reactions for an incident beam momentum of 9.9 GeV/c. This energy was chosen as a compromise between being well within the scaling domain, yet having sufficient sensitivity to cross sections which fall sharply with increasing energy. This first experiment obtained an upper limit on the $\bar{p}p$ elastic cross section which set a limit on the ratio of $R(\bar{p}p/pp) < 4\%$ at 90° c.m., and the ratio of K^-p/K^+p elastics was inconclusive. The results showed large flavor dependence for 90° scattering. Quark interchange topologies clearly dominated. The goals of the second experiment were to increase sensitivity by reducing the energy while still remaining in the scaling region, to obtain actual measurements of the suppressed cross sections, and to measure new reactions with K and $\bar{p}$ beams.

In the following sections we summarize the dimensional scaling arguments and present a formalism which expands the scattering amplitude into contributions from different valence quark topologies; we discuss the apparatus, trigger and beam, event selection and event analysis; we discuss the results of this experimental program.

THEORETICAL DISCUSSION

There have been a number of theoretical approaches to describe large angle elastic scattering. Meson exchange models include coherent multiple scattering [2] and the massive quark model [3]. QCD-based models include the hard scatter of a single fast quark [4], and the hard scattering of minihadrons [5]. In the minihadron model, the hadrons which participate in the large angle scatter have fluctuated to a size smaller than $\hbar/p_T$, the size probed by the interaction. This leads to fixed-angle scaling and color transparency [6]. In color transparency, minihadrons do not rescatter from other nucleons in the nucleus if the hard exclusive scatter takes place inside a nucleus. A large transparency effect has been observed which may be the color transparency predicted by the minihadron model [7]. The other models generally do not reproduce observed energy dependence, and do not lead to color transparency. It is for these reasons that we emphasize the minihadron model here.

In 1973, Matveev, Muradyan, and Tavkhelidze [8] and Brodsky and Farrar[9] suggested that the differential cross section for large angle elastic scattering should scale with the center of mass energy:

$$\frac{d\sigma}{dt}(ab \to ab) \underset{(t/s)\,\text{fixed}}{\underset{s\to\infty}{\sim}} \frac{1}{s^{n-2}} f_{ab}(t/s).$$

In this formalism, n equals the total number of all interacting fields, and the scaling is referred to as dimensional scaling, or constituent counting. Therefore, the observed power n measures the number of interacting fields. The minimum number for n is the sum of valence quarks in the initial and final states (e.g., 12 for baryon-baryon elastic scattering and 10 for meson-baryon scattering), leading to energy dependences of s^{-10} and s^{-8} for pp and πp elastic scattering, respectively. Experimentally, dimensional scaling has been established in pp, πp, and ep elastic scattering at fixed angles in the center-of-mass frame, fixed t/s. The power n which is observed is, indeed, approximately equal to the sum of valence quarks, indicating that sea partons are not involved in large angle exclusive scattering. pp and ep elastic scattering data indicate that the threshold for dimensional scaling begins

at incident momenta of ≈ 5 GeV/c [10, 11]. The success of dimensional scaling suggests that high p_T exclusive interactions probe the valence structure of hadrons.

Whether or not a perturbative QCD (PQCD) description of large angle exclusive reactions is justified has been debated [12]. At issue is whether the momentum transfer for the parton interactions is sufficiently large to use perturbation theory. Li and Sterman [13] have estimated the perturbative contribution to the pion magnetic form factor, after including radiative effects that prevent the quarks from separating (Sudakov suppression). They find that about half of the form factor is perturbative for $Q^2 \approx 5$ (GeV/c)^2. Additionally, Jacob and Kisslinger [14] have suggested that the asymptotic terms begin to dominate at about $Q^2 \approx 3.5$(GeV/c)^2. Spin data, however, generally disagree with a simple lowest order PQCD picture. Large transverse single-spin asymmetry for proton-proton elastic scattering [15] and a large azimuthal dependence for the decay $\rho^- \to \pi^-\pi^0$ from the 90° reaction $\pi^- p \to \rho^- p$ [16] were not expected under lowest order PQCD.

Farrar has expressed meson-baryon scattering amplitudes as a sum of terms involving valence quark scattering amplitudes [17]. The amplitudes can be subdivided into four basic categories, shown in Fig. 1, which are described by pure gluon exchange (GEX), quark interchange (INT) between the hadrons, quark-antiquark annihilation (ANN) and pair creation, or a combination (COMB) of the above. The quark scattering amplitudes within each group differ in their quark chirality, and each amplitude consists of a sum of many individual Feynman graphs corresponding to the various ways that the required gluons connect to the quark lines. The large number of two-body exclusives accessible by $\pi^\pm$ and $K^\pm$ beams on proton targets with pseudoscalar mesons in the final state have been expressed as linear combinations of

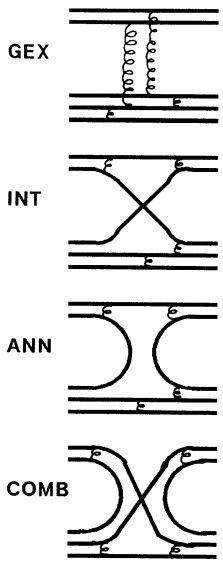

FIG. 1. The four general types of quark flow diagrams which contribute to meson-baryon, two-body exclusive reactions. The diagrams contributing to baryon-baryon reactions are similar.

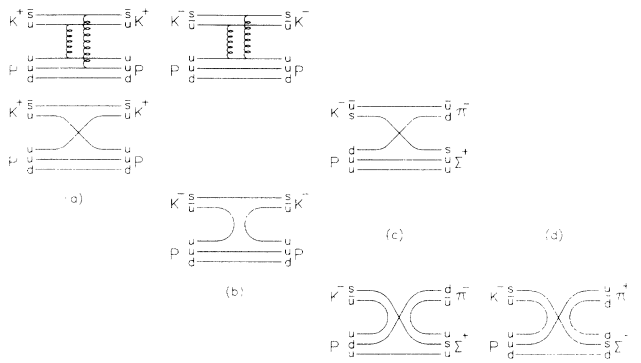

FIG. 2. Quark flow diagrams which contribute to (a) K^+p and (b) K^-p elastic scattering, (c) the reaction $K^-p \to \pi^-\Sigma^+$, and (d) the reaction $K^-p \to \pi^+\Sigma^-$.

thirteen quark scattering amplitudes. Several examples are shown in Fig. 2, with quark flavors identified for $K^\pm p$ elastic scattering and $K^-p \to \Sigma^\pm\pi^\mp$.

With this formalism, a calculation of the cross sections is possible, although this work is not complete. However, certain reactions isolate one or another category of amplitudes. By measuring a large number of reactions, it is possible to isolate the relative importance of pure gluon exchange, quark interchange, and the others. This approach was used in our 9.9 GeV experiment, and quark interchange diagrams appeared to dominate [1].

APPARATUS

Beam. A 24 GeV/c proton beam from the Brookhaven AGS with typically 4×10^{12} protons each 3 sec over a 1 sec flattop produced the C1 secondary beam from a platinum target. The C1 beam line was 100 m long from the production target to the center of our hydrogen target. The production angle was 0°; horizontal collimator jaws following a dipole magnet defined a momentum bite of $\Delta p/p \approx 1\%$ full width at half maximum (FWHM). The beam acceptance was $\Delta\Omega = 0.8$ msr. The typical secondary beam intensity was 2×10^7 particles per spill.

Beam particle type was tagged, using two differential gas Cherenkov counters located about 27 m upstream from the experiment. The counters were 1.5 m long by 0.5 m diameter, and were filled with pressurized CO_2 gas. The optics consisted of a spherical mirror at the downstream end, reflecting 5° and 8° cones of Cherenkov light to two concentric rings of six 5 cm phototubes at the focal plane. The index of refraction was adjusted by changing the pressure of the gas. The upstream counter tagged pions and kaons, and the downstream counter identified kaons and protons. Positive identification required a hit multiplicity of 4, 5, or 6 (six tubes per ring) within the proper ring in conjunction with a time-to-digital converter (TDC) value in time with the spectrometer track. Kaon identification required both kaon rings. Figure 3 shows pressure curves for the beam Cherenkov counters, taken for positive and negative beams at low intensity. The arrows indicate our standard settings. Particle type

is clearly identified, although at high intensity inefficiencies and accidentals develop for the most active rings ($\pi^{\pm}, p$). We used low intensity to determine the beam composition, which is given in Table II, corrected for particle decay to the hydrogen target position. At higher intensity, contamination was deduced from TDC distributions of summed signals from each ring.

Just upstream from the hydrogen target was a beam hodoscope, constructed of overlapping scintillation counters defining 32 3.1 mm wide bins in both horizontal and vertical projections. From this point and the beam line optics, a beam trajectory through the hydrogen target was defined. The beam at the target was 2.5 cm × 3.8 cm (H, V) with angular dispersion 10 mrad × 35 mrad, all FWHM.

A detailed measurement of the central beam momentum was accomplished by examining opening angle kinematics for pp and πp elastic scattering. By measuring the elastic opening angle, the spectrometer scattering angle, and assuming particle masses for various elastic interactions, the central beam momentum was deduced. Limited by the relative alignment of the side array with respect to the spectrometer drift chambers, the centroids of the opening angle distributions for pp and πp elastics were determined to within 1 mrad, corresponding to a ±0.5% measurement of the central beam momentum. The measured mean momentum for the positively charged beam was 5.88 GeV/c, with runs ranging within ±0.8%. The mean momentum for negative beam was 5.86 GeV/c, with runs ranging over ±0.3%. The beam momentum distribution was assumed to be Gaussian with $\sigma = 0.6\% \pm 0.1\%$ of the nominal beam momentum. This width was deduced from the spread of the opening angle distributions.

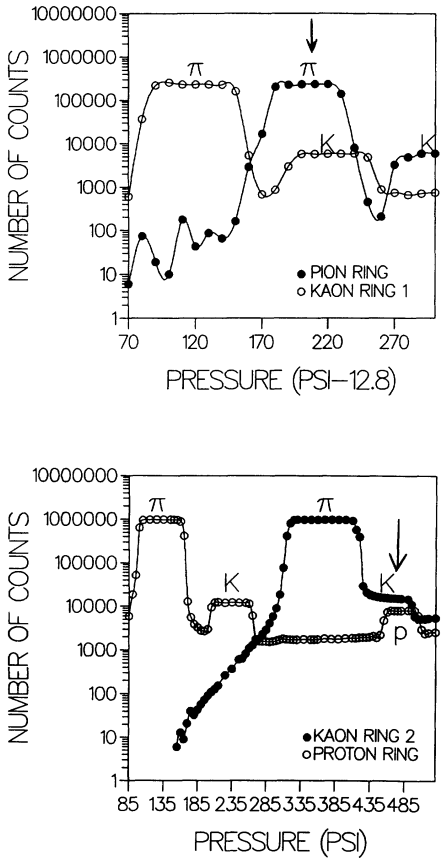

FIG. 3. Cherenkov Counter Pressure Curves. The graphs show the number of counts in the two rings of each of the two counters versus the pressure of the CO_2 gas at 5.9 GeV/c. Curve (a) indicates the counter which identified pions and kaons in a positive beam. There is a correction of 12.8 psi to the recorded pressure. Curve (b) is for the counter which identified kaons and antiprotons in a negative beam. The pressures were set at 225 psi in the pion/kaon counter, and 475 psi in the kaon/proton counter.

TABLE II. Fractional beam composition at the hydrogen target.

Particle	Positive beam	Negative beam
Protons	0.433 ± 0.010	0.009 ± 0.0005
Kaons	0.008 ± 0.001	0.008 ± 0.0006
Pions	0.525 ± 0.010	0.926 ± 0.002
Muons	0.03	0.06

Beam normalization used the scaled beam hodoscope counts (ORed) and an ion chamber with aluminum foil collecting plates, filled with an Ar-CO_2 gas mixture. In addition, we used a scintillator telescope which counted particles scattered at large angle from the target region. These monitors were scaled and written to tape after each pulse. Low intensity runs were used to accurately count the beam with the beam hodoscope, in order to normalize the ion chamber. The efficiency of the beam hodoscope was 0.985 at low intensity. The beam telescope was used to verify the linearity of the ion chamber response at high intensity, and as a cross-check of its stability.

Target region. A schematic of the target and spectrometer is shown in Fig. 4. The liquid hydrogen target was built using a thin (0.8 mm) aluminum shell supporting a cylindrical Mylar flask measuring 99 cm in length and 10 cm in diameter. The flask was surrounded by low density insulation and kept in vacuum. To minimize beam scatter, the upstream end of the shell contained a 0.3 mm Mylar entrance window. Veto counters were positioned above and below the target to reduce triggers from inelastic interactions.

Spectrometer. The spectrometer arm consisted of four multiwire drift chambers, a dipole analyzing magnet, five scintillator hodoscopes, and a threshold Cherenkov counter. Capable of pion identification, accurate determination of momentum and scattering angle, the spectrometer also functioned as the event trigger. An AGS 48D48 dipole magnet, with 122 cm vertical and 46 cm horizontal apertures, was mounted to bend vertically. Operating with a central field strength of 1.284 T, and an effective field length of 152 cm, the magnet gave a vertical momentum kick of 0.585 GeV/c to charged particles. For elastic events, this impulse corresponded to about 10° of vertical bend.

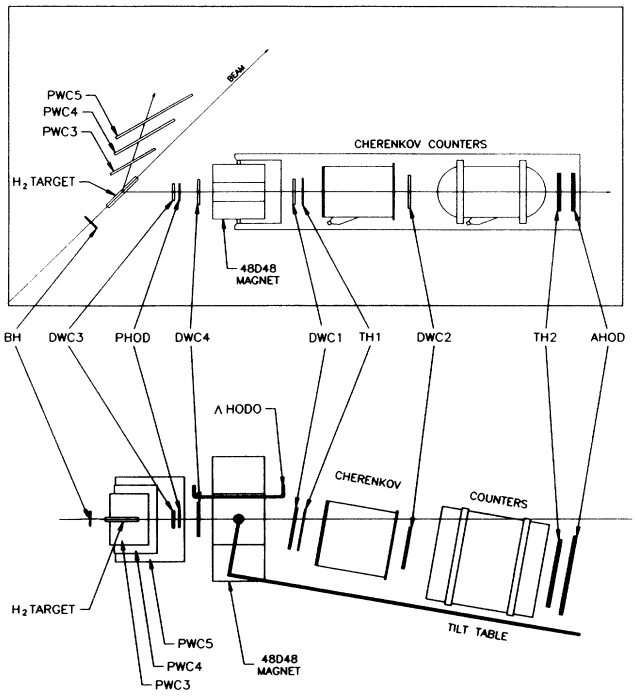

FIG. 4. Detector apparatus for E838. Plan view (a) and elevation view through the center line of the spectrometer (b). The scintillation counters include: a beam hodoscope (BH), trigger hodoscopes (PHOD,TH1,TH2,AHOD, and ΛHODO), and veto counters above and below the hydrogen target (not shown). There are wire chambers (DWC3, DWC4, DWC1, and DWC2) in the spectrometer and in the side array (PWC3, PWC4, and PWC5). The liquid hydrogen target and the side array were fixed with respect to the beam, and the spectrometer rotated horizontally about the target center. The tilt table allowed vertical adjustments for the 48D48 bend angle.

Low momentum negative particles which did not completely traverse the magnet were deflected upward into the Λ hodoscope, ΛHODO, mounted on the top inner surface of the magnet (see Fig. 4). The hodoscope consisted of six 199 cm long, 7.62 cm wide elements with photomultipliers on both ends. Signals from both phototubes were latched and timed. The time difference from the photomultiplier tubes PMT's gave the position of the π^- along the spectrometer axis (z). We could infer the z position to within $\sigma = 9.7$ cm according to calibration studies. These positions enabled us to find particle momenta to 5%. Downstream of the magnet, a pressurized threshold Cherenkov counter detected spectrometer pions. A second, atmospheric, spectrometer Cherenkov counter was used in E755, but not for the lower energy experiment.

A series of four drift chamber modules aligned along the spectrometer axis provided accurate tracking information on particles traversing the spectrometer arm. Adjacent planes were staggered by half a wire spacing. Overall, the position resolution for the drift planes was 0.02 cm. The momentum resolution was $\sigma = 1\%$ and scattering angles were measured to $\sigma = 2$ mrad. These errors were dominated by multiple Coulomb scattering.

Four scintillator hodoscopes were used to observe the spectrometer track: PHOD upstream and TH1, TH2, AHOD downstream. These were used in the fast trigger, and TH1 set the event time.

Three large proportional chambers made up a side array designed to track particles from various elastic interactions, or to track charged decay products from unstable resonances. These chambers measured coordinates (X, U, V) for proportional wire chamber 3 (PWC3), (U, V) for PWC4, and (U, V) for PWC5. The $U(V)$ wires were strung at $-29°(+29°)$ from the vertical, and the X wires were strung vertically. Chamber resolution for the side arm was 0.08 cm, and track angles were measured to within 4 mrad. Detector sizes and positions are given in Table III.

Trigger. For E838, the principal event trigger used three requirements. The first trigger stage required a charged particle to traverse the spectrometer arm, firing at least one element in each of the four trigger hodoscopes, and was called a 4 out of 4, or 4×4. The second and third trigger stages were designed to eliminate most of the inclusive background by selecting events with a stable particle (π, K, or p) passing through the spectrometer above a minimum momentum. The second stage trigger (HMAT) used two scintillator hodoscopes and, thus, had excellent time resolution (10 nsec) and moderate momentum resolution ($\Delta p/p = 21\%$); the third stage trigger (DMAT) used latched wire hits from two drift chamber modules and had momentum resolution $\Delta p/p = 11\%$ and time resolution 150 nsec. In addition, the devices observed the track at three spatial points (TH1/DWC1, DWC2, TH2/AHOD) which further reduced the accidental trigger rate from multiple low momentum tracks which could mimic one high momentum track. HMAT consisted of a hardware matrix which compared observed TH1×TH2 hits within the 10 nsec coincidence window to allowed TH1×TH2 hit combinations, set to cover the desired secondary momentum bite. DMAT consisted of four matrices which allowed different momenta to be accepted by the trigger for different scattering angles, as defined by AHOD, and for the Λ trigger. Observed DWC1×DWC2 hits were compared with allowed combinations for wire hits that were within the drift time window for each chamber (DWC1: 75 nsec; DWC2: 150 nsec). The sample of events formed from this trigger was independent of the decay properties of the other final state particle. It was this feature which allowed the simultaneous collection of so many reactions.

An additional trigger was used to find exclusive Λ^0 interactions. Detectable Λ decayed into high momentum protons that traversed the spectrometer arm and low momentum pions that were deflected upward into ΛHODO. The Λ trigger required a hit in ΛHODO in coincidence with a 4×4. A unique DMAT matrix was used, corresponding to the expected proton momentum range. AHOD was not used in the Λ trigger.

Data acquisition. The first level trigger (4 × 4) initiated the digitization for TDC's and analogue-to-digital

TABLE III. Detector sizes and positions. The x (y) planes measured horizontally (vertically); the u and v measurements were along axes inclined $\pm 29°$ from horizontal. DWC's (PWC's) were drift (proportional) wire chambers. PHOD, TH1, TH2, AH, ΛHODO, were scintillation counter hodoscopes. The analyzing magnet (48D48) center and ΛHODO center along the z axis are indicated. The side arm chambers were 14° to the beam and the distances to the target are from the target center, perpendicular to the chambers. PWC5 covered a range of scattering angles from 10° to 52° from the center of the target.

Device	Size (cm) $(x \cdot y)$	Cell size (cm)	Measuring planes	Distance to target (cm)
Spectrometer arm ($-27°$ from beam)				
DWC3	42×42	0.32	x,x,y,y	140
PHOD	39×42	11.4(3,7.6(1)	y	180
DWC4	61×83	0.32	u,x,y,y	269
48D48	46×122	Aperture	—	$c = 432$
ΛHODO	$46(x) \times (199)(z)$	$7.6(x)$	x,z	$c = 447$
DWC1	60×102	0.64	x,x,v,y,y	592
TH1	67×102	12.7	y	630
DWC2	81×102	1.27	x,x,y,y	846
TH2	91×173	10.2	y	1224
AH	92×193	30.5	x	1240
Side arm ($+10°$ to $52°$ from beam)				
PWC3	123×90	0.32	x,u,v	48
PWC4	164×100	0.32	u,v	86
PWC5	205×161	0.32	u,v	117

converters (ADC's), and generated a 2.5 μsec local dead time. The rate of this trigger was about 1000 Hz. The second and third level triggers (HMAT × DMAT) either initiated the read-out cycle (about 3 msec long) or canceled the trigger and cleared the digitizers. The final event rate with full beam was about 70 Hz, with about 20% dead time. The data consisted of latched hit information (trigger type, beam and spectrometer Cherenkov PMT's, hodoscope PMT's, side chamber wires), scaler numbers (beam monitors, including dead time information), TDC's (beam Cherenkov rings, hodoscopes, drift chambers), and ADC's (spectrometer Cherenkov). A PDP 11/60 computer with the MULTI data acquisition system from Fermilab was used to write the data to magnetic tape and to monitor the experiment. Runs were taken with positive and negative beams, and with both polarities of the spectrometer magnet, as well as target empty data and calibration data with different trigger conditions. The results given here are based on a 500 hour run in 1988.

Track reconstruction. E838 software was designed to look for one or two tracks in the spectrometer and up to three tracks in the side arm. If there were enough hits to reconstruct a spectrometer track through the magnet, all possible combinations of two hits were made separately for x hits, y hits downstream of the magnet, and y hits upstream of the magnet. The x and y tracks with the greatest number of hits were then combined. The spectrometer track was chosen on the basis of the greatest number of hits and minimum χ^2, with the requirement that the two y tracks meet in the center of the magnet. Hits which were not used in the through track were checked for a possible track upstream of the magnet. If there were at least 2 unused x and 2 unused y hits, tracks were found as in the through track reconstruction. The reconstruction was done similarly in the side's u and v planes. A minimum of one hit in each of four planes in the side chamber was required to make a track.

ACCEPTANCE CALCULATION

Geometric acceptance, trigger and apparatus efficiencies, reconstruction efficiency, and the efficiency of kinematic cuts used in event selection are needed to obtain cross sections from the raw data. These were obtained from the data and from a Monte Carlo simulation.

Trigger efficiency was measured from data sets taken with less restrictive triggers and from simulation. Although the drift matrix DMAT proved to be efficient, the hodoscope matrix was inefficient for high momentum tracks. This bias in the trigger resulted in event loss being both angle and incident beam dependent. Examination of special trigger runs (with HMAT disabled) confirmed the scale of the error (about a 10% reduction in the pp elastic sample). All Monte Carlo acceptance calculations included the effects of the hodoscope matrix upon raw data selection.

Apparatus efficiencies were obtained from the abundant and overconstrained pp and πp data. Hodoscope efficiencies were >96%, as were drift plane efficiencies in the magnet arm. Wire plane efficiencies in the side arm were 90–98 %.

Efficiencies for kinematic cuts used to select events were measured using overconstrained data, as well as by simulation. For example, pp elastics could be selected without information from the side array. Select-

ing events based on Cherenkov identification and missing mass alone, a signal to background ratio of 12:1 was observed for pp elastic events (6:1 for $\pi^- p$ elastics). The efficiencies for kinematic cuts involving the side array were determined by examining the pp and $\pi^- p$ signal sizes before and after applying kinematic constraints. The results indicate that 32% ± 3% of elastic events failed to satisfy basic event selection (coplanarity, opening angle, and common event vertex within the target volume). The error associated with this correction is dominated by uncertainties in the missing mass background subtraction. The inefficiency was due to insufficient redundancy in the side array tracking, after taking into account wire plane efficiencies and noise hits. This inefficiency did not depend on angle.

A study of hits that were not used by the side reconstruction indicated a complicated correlation between hits from different layers and the reconstructed track. The consequences of this were sharply varied efficiencies for events depending on the number of planes used in the fit and the number of unused hits remaining after reconstruction. Events in the pp mass peak with 7 of 7 side planes used in the fit, and with fewer than 2 unused hits were 98% ± 2% efficient at passing all kinematic cuts. Events with 5 side hits used in the fit and 2 or more unused side hits were only 38% ± 5% efficient at passing all kinematic cuts. A study indicated no significant angular difference between the 7 hit high efficiency sample and the total sample. Because of statistical limitations on several of our measurements, we were unable to cut hard on these parameters. We chose to exploit the large signal to background ratio observed for pp and $\pi^- p$ elastics to measure the overall efficiency.

A Monte Carlo simulator was used to obtain the event acceptance. Factors included in the simulation were geometry, software simulation of the hodoscope and drift chamber triggers, reconstruction algorithm efficiency, wire plane efficiencies, multiple scattering, random noise hits, target absorption, and particle decay. Calculating the acceptance was accomplished by dividing the number of events successfully reconstructed by the total number of events generated.

Both isotropic decays and polarized decays were considered for the ρ, Λ, and Δ. Quoted systematic errors include acceptance errors from lack of information on polarization.

Observed wire plane efficiencies were simulated by eliminating hits at random such that the Monte Carlo efficiencies matched the observed efficiencies. In addition, dead wires or regions of high hardware inefficiency were included explicitly. Finally, noise hits were added to the accumulated hit lists in an attempt to model spurious noise. Hodoscope hits were recorded so that the Monte Carlo stimulator could simulate the hodoscope trigger HMAT. Similarly, drift chamber hits were used to model the drift trigger DMAT.

Event reconstruction of simulated data used the same software as the real data. This ensured that any systematic errors attributed to the reconstruction software would be accounted for in the acceptance.

Figure 5 shows the pp elastic acceptance, as determined by the Monte Carlo simulation.

EVENT ANALYSIS

We will discuss here the event selection, grouped by similar selection criteria. The observed numbers of events for each reaction and cross sections are given in the Appendix.

$pp \to pp, \pi^\pm p \to \pi^\pm p$. These elastic events were selected using missing mass, coplanarity, and opening angle, along with a common event vertex in the target volume and the appropriate beam Cherenkov counter identification. The missing mass distribution for $pp \to p + X$ is shown in Fig. 6. Nearly 100 000 pp elastics were selected using opening angle and coplanarity cuts, with all events within 3σ of the proton mass included. Event contamination was estimated at <0.1%. The high statistics allowed a detailed measurement of the t dependence of the pp elastic cross section near 90° c.m., as presented later in this paper.

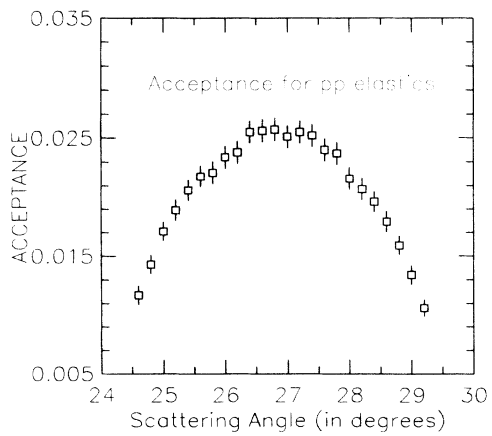

FIG. 5. Fractional acceptance for pp elastic scattering as a function of the lab scattering angle.

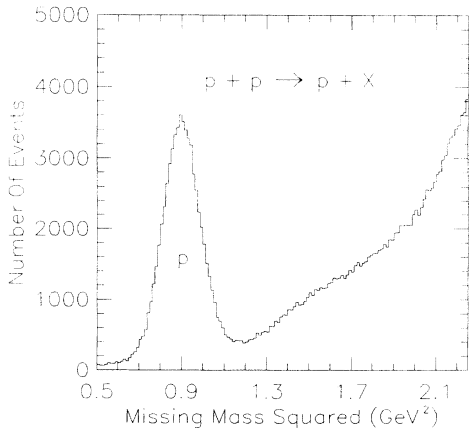

FIG. 6. Missing mass squared plot for the reaction $pp \to pX^+$. This very large sample of events allowed many systematic studies.

Figure 7(a) shows the opening angle plot for $\pi^+p \to (p \text{ or } \pi^+)X$ and Fig. 7(b) shows the data where the spectrometer Cherenkov identified a π^+. The $\pi^+p \to p\pi^+$ (proton in spectrometer) and $\pi^+p \to \pi^+p$ (π^+ in spectrometer) are clearly identified. It can also be seen that the spectrometer Cherenkov efficiency was high (91%), and the fraction of false signals (p identified as π^+) is small (4%). A precise measurement of the spectrometer Cherenkov efficiency was determined from π^-p elastic events with the spectrometer magnet polarity set for negatives (π^- in the spectrometer). Figure 8(a) shows the missing mass for $\pi^-p \to \pi^-X$ and Fig. 8(b) shows $\pi^-p \to pX$. For π^-p elastics, beam Cherenkov identification was not necessary, since the negative beam is dominantly π^-. In the case of Fig. 8(a), the spectrometer polarity was reversed—a majority of the data was taken with positives deflected downward. After selection cuts we collected 8100 π^+p elastics and 22 400 π^-p elastics. The cross sections, binned in t, are given in the Appendix.

$K^\pm p \to K^\pm p$. For K^+p elastics, the spectrometer Cherenkov could not distinguish between protons or K^+. For our scattering angle range of 25.5° to 28.5° in the laboratory, the range in t for the two cases overlapped: $-t = 4.2$ to 4.8 $(\text{GeV}/c)^2$ for $K^+p \to K^+p$ where the K^+ was in the spectrometer, and $-t = 4.7$ to 5.4 $(\text{GeV}/c)^2$ for $K^+p \to pK^+$. Candidate events were accepted if they satisfied (pK) or (Kp) elastic kinematics, and missing mass calculations assumed (pK) (proton in spectrometer). The missing mass squared shift for misidentified (Kp) events was 0.05 GeV^2. Figure 9(a) shows the $K^+p \to pX$ missing mass distribution. 88 events were observed, with an expected background of 8 events from mostly π^+p elastics. The cross-section calculation assumed that we observed the sum of (pK) and (Kp) events.

For K^-p elastics, the spectrometer particle is unambiguous; however, the contamination from π^-p elastic accidental background is larger. Figure 9(b) shows the $K^-p \to pX$ missing mass distribution for a tight timing cut on the beam Cherenkov rings; Fig. 9(c) shows the TDC distribution for one kaon ring for K^-p elastics with a looser timing cut. The K^-p elastics have the correct event time for the kaon rings, and the out-of-time data are from π^-p elastic events with an accidental kaon in the beam. The background from π^-p elastics in the event window can be estimated directly from the timing plot. With the final cuts, we identified 22 ± 7 K^-p elastic events.

$\bar{p}p \to p\bar{p}, \pi^+\pi^-, K^+K^-$. An antiproton in the beam was identified as a positive signal from the proton beam Cherenkov ring, and no in-time signal from the pion ring. About 1% of the negative beam consisted of antiprotons. Figure 10(a) shows the missing mass for $\bar{p}p \to pX$, and Fig. 10(b) shows $\bar{p}p \to \bar{p}X$ for runs with negative spectrometer polarity. We observe 148 events, with an estimated <2% background. We note we were only able to set an upper limit on this reaction at 9.9 GeV/c.

We show in Fig. 11(a) the missing mass for events with a π^+ in the spectrometer Cherenkov, $\bar{p}p \to \pi^+X$, and in Fig. 11(b) for the spectrometer Cherenkov in pion veto (p or K^+), $\bar{p}p \to K^+X$. Because of the very large center-of-mass momentum of the two-body final states, the $\bar{p}p \to \pi^+\pi^-$ and K^+K^- reactions are clearly separated from any background. We observe 6 and 2 events, respectively. The trigger for these high momentum reactions was not efficient, so the acceptance was much lower than for elastics.

In addition to the eight reactions discussed above, twelve interactions were also measured which included final state particles with short lifetimes. The reactions listed in Table I with ρ, Δ, K^*, Σ, Λ, or K^0 final states could not generally be selected using coplanarity or opening angle. Backgrounds were more difficult to determine in these reactions. In order to make a quantitative measurement, backgrounds needed to be parametrized and subtracted. Acceptance of charged decay products in the side array was complicated by the possibility that the ρ and Δ resonances did not decay isotropically. Despite these complications, the reaction signatures were clear and distinct.

$\pi^\pm + p \to p + \rho^\pm$. The first resonance to be considered, the $\rho(772)$, was measured in both positive and negative data. Basic event selection required pion identification in the beam (for positive data only), the absence of a pion Cherenkov signal from the spectrometer counter, a single track in the side array from $\rho^\pm \to \pi^\pm\pi^0$ decay, and an event vertex within the target volume.

Plots of the missing mass squared (Fig. 12) reveal a large elastic peak near zero mass, corresponding to πp elastics. The mass squared distributions also clearly indicate a large excess of events around the ρ mass in both

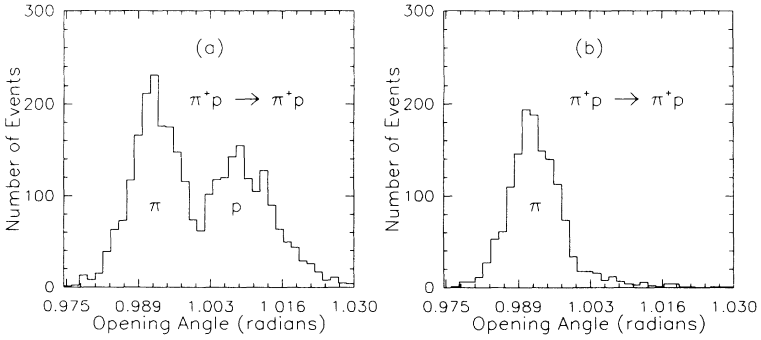

FIG. 7. This is a plot of opening angle for π^+p elastic events. (a) has no spectrometer Cherenkov identification and shows peaks corresponding to whether a proton or a pion traversed the spectrometer. (b) displays the same distribution with π^+ identification.

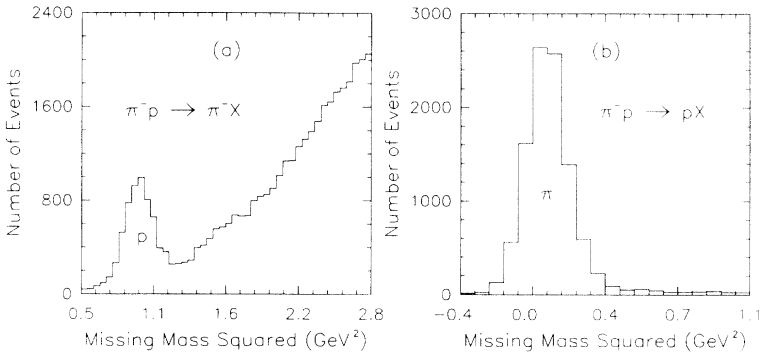

FIG. 8. Missing mass squared plots for $\pi^- p$ with (a) no angle cuts for pions in the spectrometer and (b) for protons in the spectrometer with elastic angle selection.

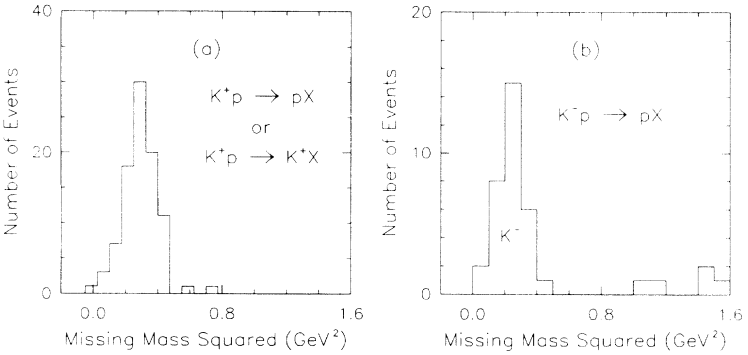

FIG. 9. Plots of missing mass squared for $K^{\pm} p \rightarrow pX$ for (a) $K^+ p$ and (b) $K^- p$ elastic candidates. For $K^+ p$ there is an ambiguity as to whether the K^+ or p is detected in the spectrometer. The $K^- p$ elastic events were selected on the basis of the timing of the first Cherenkov ring as shown in (c).

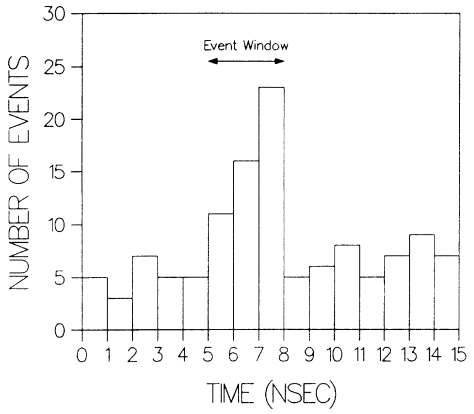

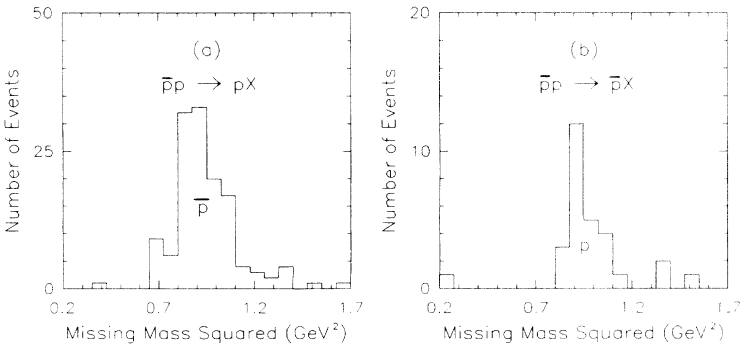

FIG. 10. $\bar{p}p$ missing mass squared distributions. Data accepted using the positive polarity of the spectrometer magnet, $\bar{p}p \rightarrow pX$ is shown in (a). (b) shows data with the polarity reversed, for $\bar{p}p \rightarrow \bar{p}X$. In both plots the angle of the side array particle was selected for elastic kinematics.

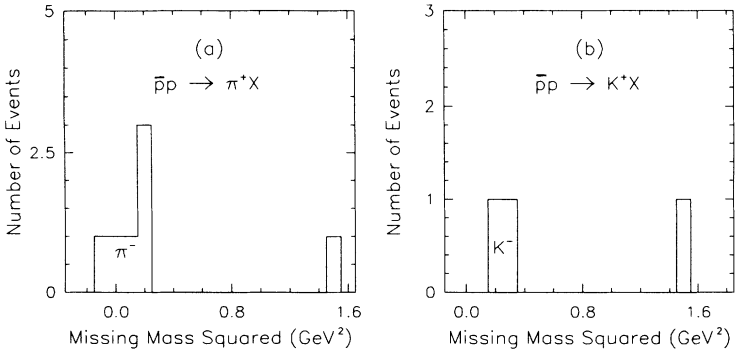

FIG. 11. Plots of the missing mass squared for events with the correct angular correlations for (a) $\bar{p}p \rightarrow \pi^+\pi^-$, and (b) $\bar{p}p \rightarrow K^+K^-$.

the positive and negative data. Determining the size of the signal required a parametrization of the mass distribution. The ρ signal shape was determined from Monte Carlo studies, while the elastic signal shape was determined from data. The inclusive background was modeled separately by two polynomial functions of the form

$$f(x) = k_1 + k_2(x - k_5) + k_3(x - k_5)^{k_4}$$

and

$$f(x) = k_1 + k_2(x - m_\pi^2) + k_3(x - m_\pi^2)^2 + k_4(x - m_\pi^2)^3 ,$$

where k_n were fitting parameters and x corresponded to the value of the square of the missing mass. The fit quality for the entire mass spectrum (elastic peak, ρ resonance, and background function) averaged over 14 separate plots was $\chi^2/N_{\rm DF} = 1.15$. The observed signal sizes were not dependent upon the form of the background function. Also note that a shoulder appeared in the positive data around a mass squared of 1.7 GeV^2. This corresponds to the $a_2(1320)$ meson. The proximity of the signal to the edge of the trigger acceptance precluded an accurate measurement of the a_2 meson cross section, although it appears that the exclusive reaction $\pi^+p \rightarrow pa_2^+$ is not greatly suppressed.

Acceptance values were derived from Monte Carlo simulations. A large number of events of the form $\pi^\pm p \rightarrow \rho^\pm p$ were generated, with the ρ meson decaying into a $\pi^\pm\pi^0$ pair. The most important factor in the calculation was experimental geometry. Complicating the acceptance process was the observed nonisotropic decay distribution of the ρ meson. Previous measurements at 9.9 GeV/c [16] and preliminary studies at 5.9 GeV/c (see C. White, Ph.D. thesis, University of Minnesota, 1990) indicate ρ decay structure. One Monte Carlo parametrization assumed complete polarization of the ρ meson, while a second assumed an isotropic decay distribution. Acceptance values were calculated for both, with the acceptance for polarized decays being 10% larger than for isotropic decays. The experimental acceptance was chosen to be the average between the two values with an error equal to half the difference between them.

Contamination of the ρ signal occurred through two primary channels, pp elastics and pion induced Δ production, $\pi p \rightarrow \pi\Delta$. Containing and estimating the Δ contamination relied upon pion identification with the spectrometer Cherenkov counter. Final background estimates were 180 events in the negative and 80 events in the positive rho data samples. The elimination of pp elastics was accomplished by making a combined cut on opening angle and coplanarity. Any event with an opening angle within 12 mrad of the value expected for pp elastics and having a coplanarity between -0.016 and 0.016 was removed. Fewer than 100 pp elastic events remained following this suppression. Reduction in the ρ acceptance was modeled by the Monte Carlo simulation, and was found to be less than 1%.

In total, approximately 6000 $\pi^+p \rightarrow p\rho^+$ and 20 000 $\pi^-p \rightarrow p\rho^-$ events were observed. Cross sections, binned in t, are given in the Appendix.

$\pi^-p \rightarrow \pi^+ + \Delta^-, \pi^\pm p \rightarrow \pi^\pm + \Delta^+$. The analysis for these reactions mirrored that used on the ρ, except that Δ event selection demanded a spectrometer pion Cherenkov identification. The missing mass squared dis-

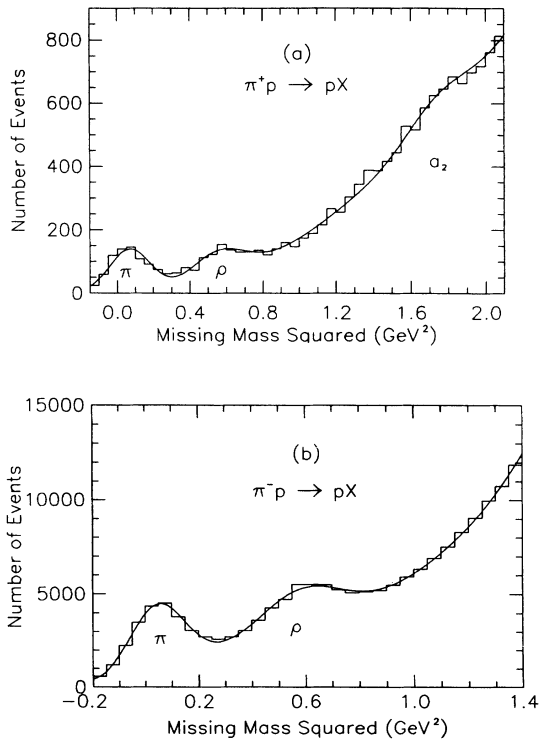

FIG. 12. Missing mass squared distribution for (a) the reaction $\pi^+p \rightarrow pX$ in which the structures corresponding to π^+, ρ^+ and a possible a_2^+ are seen. A similar plot for $\pi^-p \rightarrow pX$ is given in (b).

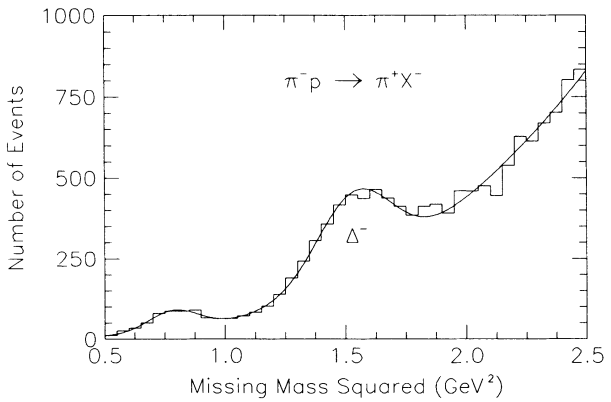

FIG. 13. Plots of missing mass squared for $\pi^- p \rightarrow \pi^+ X^-$. The small bump at 0.7 GeV^2 is due to $\pi^- p$ elastic events where the spectrometer proton has been misidentified as a pion. The other peak corresponds to the reaction $\pi^- p \rightarrow \pi^+ \Delta^-$.

tribution for the reaction $\pi^- + p \rightarrow \pi^+ + X$ is shown in Fig. 13. The Δ^- peak is evident, and the lower mass peak is from $\pi^- p$ elastic events where the spectrometer proton was misidentified as a pion. A fit including background (as for the ρ fits) gave 5810 $\pi^- p \rightarrow \pi^+ \Delta^-$ events with $\chi^2/N_{\mathrm{DF}} \approx 0.9$. Results for cross sections for four scattering angles are given in the Appendix.

For the Δ^+ we also used a maximum opening angle cut for the $\Delta^+ \rightarrow p\pi^0$ decay, ignoring $\Delta^+ \rightarrow \pi^+ n$ decays which have a large opening angle and poor acceptance. The Δ^+ direction is determined from the beam and spectrometer momenta, and the charged daughter track is observed in the side chambers. The uncertainty in the Δ^+ angle was 12 mrad and the uncertainty in the decay angle was 13 mrad. The maximum decay opening angle is 90 mrad for this energy. Figure 14(a) shows the missing mass squared distribution for "standard" cuts, and Fig. 14(b) shows the distribution after the decay opening angle cut (<150 mrad) is applied, along with elastic suppression cutting on opening angle and coplanarity. The fit gave 1540 $\pi^+ p \rightarrow \pi^+ \Delta^+$ events with $\chi^2/N_{\mathrm{DF}} = 28/28$.

The same analysis was used for $\pi^- p \rightarrow \pi^- \Delta^+$ event selection. The missing mass plot, after elastic suppression and the decay angle cut, is shown in Fig. 14(c). A fit to the missing mass distribution without the tight decay angle cut gave 1200 events with $\chi^2/N_{\mathrm{DF}} = 24/20$.

As with the ρ, the Δ decay distribution may not be isotropic. Several Monte Carlo runs simulated the observed decay distribution as well as an isotropic distribution. The general geometric acceptance was calculated as before with the decay angle cut applied after reconstruction. The difference in the acceptance between the polarized and isotropic decay modes is small (less than 5%).

$K^+ p \rightarrow pK^{*+}, K^+ p \rightarrow K^+ \Delta^+$. Separation of these reactions is complicated by our inability to distinguish between protons and kaons in the spectrometer. The missing mass squared distributions for the two reactions differ by only 0.07 GeV^2, if the K^+ is misidentified as a proton. The distribution for $K^+ p \rightarrow pX$ is shown in Fig. 15. The events in the peak labeled "K^*" can in-

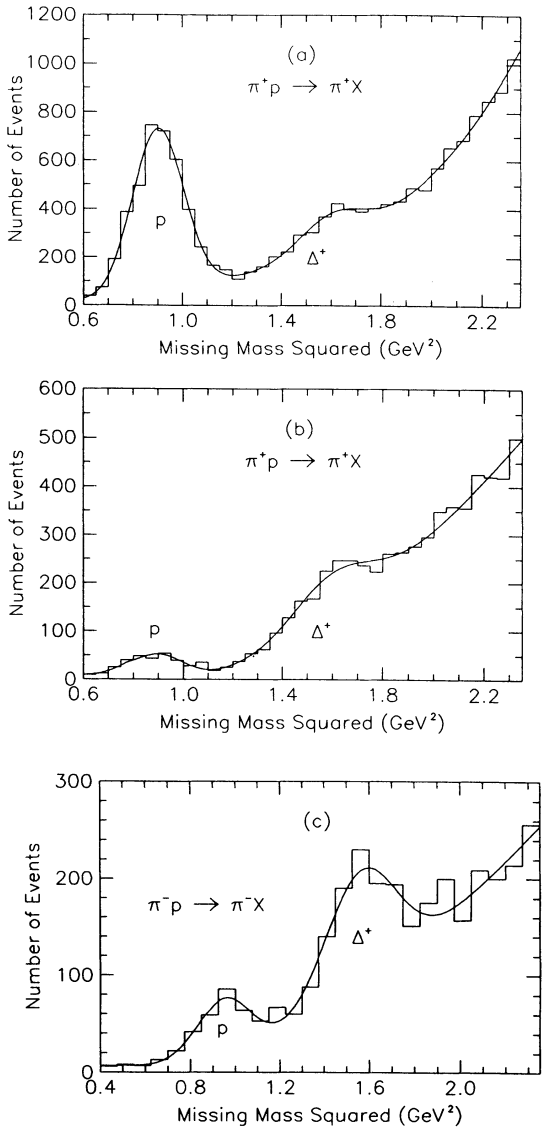

FIG. 14. Fitted missing mass squared plots for the reaction $\pi^+ p \rightarrow \pi^+ X^-$ with (a) minimal selection and (b) elastic suppression with decay angle cuts. (c) is the plot for the reaction $\pi^- p \rightarrow \pi^- \Delta^+$ with elastic suppression.

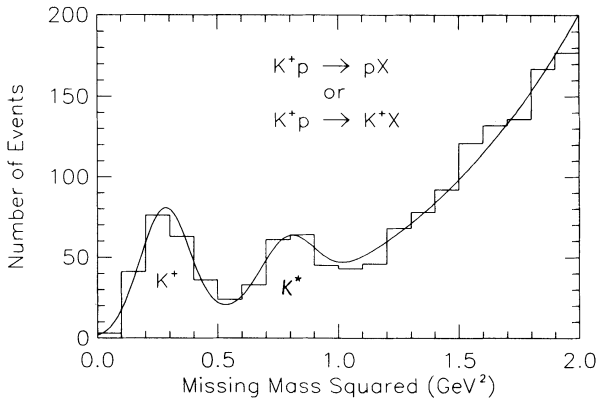

FIG. 15. Missing mass squared distribution for $K^+ p \rightarrow pX$. Since there was no kaon identification in the spectrometer, the distribution is a combination of $K^+ p \rightarrow pX^+$ and $K^+ X^+$. See text for details.

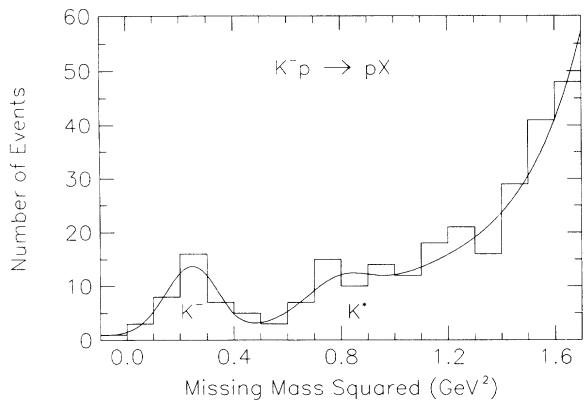

FIG. 16. Missing mass squared plot defined by $K^-p \to pX^-$. The shoulder at 0.8 GeV^2 indicates the reaction $K^-p \to pK^{*-}$.

clude both K^* and Δ reactions. We have used the decay angles to separate the reactions. Our side chambers accept mainly the decays $K^{*+} \to K^+\pi^0$ and $\Delta^+ \to p\pi^0$. The maximum opening angle for the proton from the Δ is 0.09 rad; for the K^+ this maximum angle is 0.14 rad. Our resolution for this angle is 0.013 rad. We observed 36 events with the decay opening angle $0.11 < \psi < 0.15$, which selects mainly K^{*+} events. We observed 39 events for $0 < \psi < 0.11$, which selects both K^{*+} and Δ^+ events. We had approximately equal acceptance for the K^{*+} in both opening angle regions. The Δ^+ acceptance is four times larger for $\psi < 0.13$. We observe roughly equal numbers of events in the two regions. Therefore, we find that the data are consistent with a K^{*+} signal and no Δ^+ signal. The acceptance did not depend strongly on whether the decay was polarized or not. Cross sections are given in the Appendix.

$K^-p \to pK^{*-}$. Without the complexities seen in K^{*+} production, $K^-p \to pK^{*-}$ was easily identified. The shoulder in the missing mass squared plot for $K^-p \to pX$ data (Fig. 16) implies a small but measurable K^{*-} signal. The fitting process gave 35^{+15}_{-10} events with $\chi^2/N_{\rm DF} = 0.8$. Eleven contaminating $\pi^-p \to \rho^-p$ events were subtracted.

$K^-p \to \pi^-\Sigma^+, K^-p \to \pi^+\Sigma^-$. Σ reactions were identified using standard particle identification (K in beam, π in spectrometer) and spectrometer scattering angle requirements, with additional cuts on the side track demanding consistency with the $\Sigma^+ \to p\pi^0$ or $\Sigma^- \to n\pi^-$ kinematics. For the Σ^+, the proton decay mode was used, requiring a decay angle $\psi < 0.12$ rad, and the distance of closest approach between the side track and the spectrometer track had to be consistent with resolution (d <3 mm in xz, and <35 mm in y). Figure 17(a) shows the missing mass squared distribution for $K^-p \to \pi^-X$, with "standard" selection; Fig. 17(b) shows the distribution with the additional requirements on the side track. A clear $K^-p \to \pi^-\Sigma^+$ signal is observed. We estimate that about one misidentified πp elastic event is expected near 1.05 GeV^2. We have assumed the background shape to be the same as for other reactions, and estimate a 1±1 event background in the 9 event Σ^+ peak.

Figure 18 shows the missing mass squared distribution for $K^-p \to \pi^+X$, with the standard cuts described above. An excess of events is observed around the Σ^- mass as indicated. We have studied the kinematics of the observed tracks for this mass region, and the events are consistent with a wide angle $\Sigma^- \to n\pi^-$ decay. We do not have sufficient resolution to separate the interaction vertex and the decay vertex. We estimate a background of four events in the nine event peak.

$\pi^-p \to \Lambda K^0, K^-p \to \Lambda\pi^0$. The decay length for a Λ is comparatively short, and virtually all Λ's decay between the target and the first trigger hodoscope, PHOD. We looked for reactions where the Λ decayed to charged particles, $\Lambda \to p\pi^-$. The signature for these reactions required two tracks in the upstream region of the spectrometer, one downstream high momentum track (the proton), and one track which curled upward in the spectrometer magnet and hit the Λ hodoscope (the π^-). The side topology required no tracks in the side arm, consistent with $K_S \to \pi^0\pi^0$, K_L, or $\pi^0 \to \gamma\gamma$; or two tracks in the side arm, consistent with $K_S \to \pi^+\pi^-$.

Tight cuts on track quality eliminated most of the background in the distribution of the effective mass of Λ candidates. Histograms are shown for both the Monte Carlo and the π^- beam data in Fig. 19. A clear peak is seen in the data with a width and mean comparable to that of the Monte Carlo data, although the shape of the background under the peak is not well known. There were approximately 200 events within the peak at the Λ mass squared for the π^- beam data. There were only 3

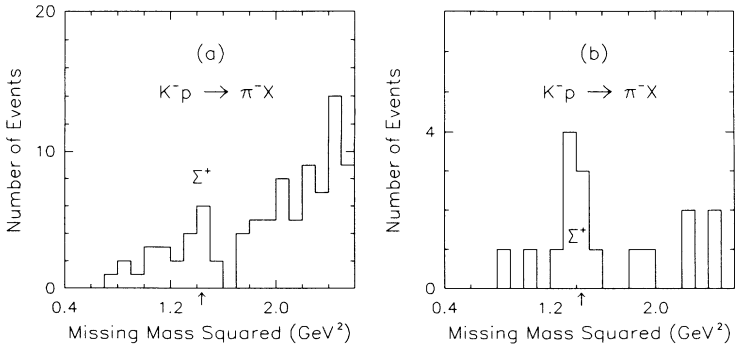

FIG. 17. The reaction $K^-p \to \pi^-\Sigma^+$ can be seen here where a kaon has been identified in the beam, and a pion in spectrometer. (a) shows events with limited selection cuts while maximum selection cuts have been applied to the events in (b).

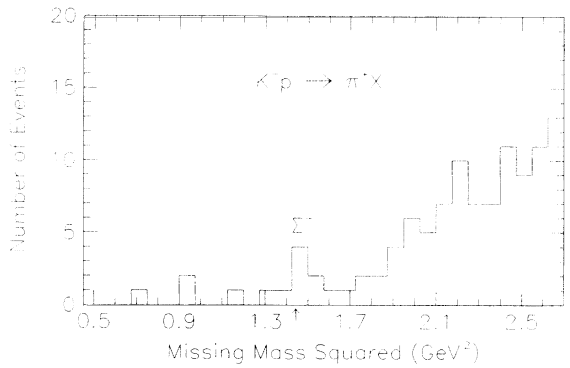

FIG. 18. Missing mass squared for $K^-p \rightarrow \pi^+X^-$ events. Minimal selection cuts have been applied to these events.

events within the Λ mass region for the K^- beam data.

The magnitude of the daughter π^- momentum used in the calculation of the missing mass of the recoil particle was derived from the true Λ mass and the measured daughter proton momentum. Histograms of missing mass squared for π^- beam events are shown in Fig. 20. Figure 20(a) is a histogram of the missing mass from the Monte Carlo data. Figure 20(b) has cuts imposed to extract Λ's, including a Λ mass cut. This plot is dominated by background, and was used to find the shape of the background for comparison with the final data sample, shown in Fig. 20(c), which was additionally cut on zero or two tracks in the side arm. This plot is consistent with the background shown by Fig. 20(b). Therefore, we have set an upper limit for this reaction. From the Monte Carlo simulation we define a missing mass squared window of -0.1 to 0.5 GeV^2 for the $\pi^-p \rightarrow \Lambda K^0$ reaction. The fraction of background events in this window in Fig. 20(b), compared to the mass region from 0.5 to 1.0 GeV^2, was 38%. From this, we estimate a background in the -0.1 to 0.5 GeV^2 window in Fig. 20(c) of 5 events. We observe 5

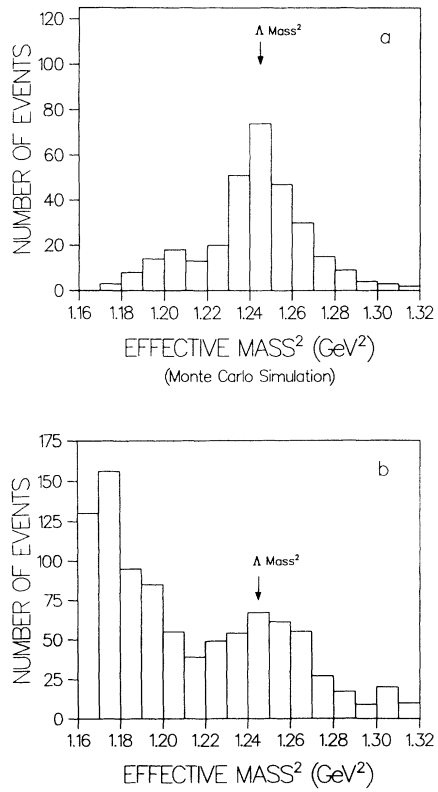

FIG. 19. Effective mass of the Λ. (a) The effective mass of the Λ from Monte Carlo simulation of $\Lambda \rightarrow \pi^-p$ events. (b) The effective mass of the Λ is shown for $\Lambda \rightarrow \pi^-p$ candidates.

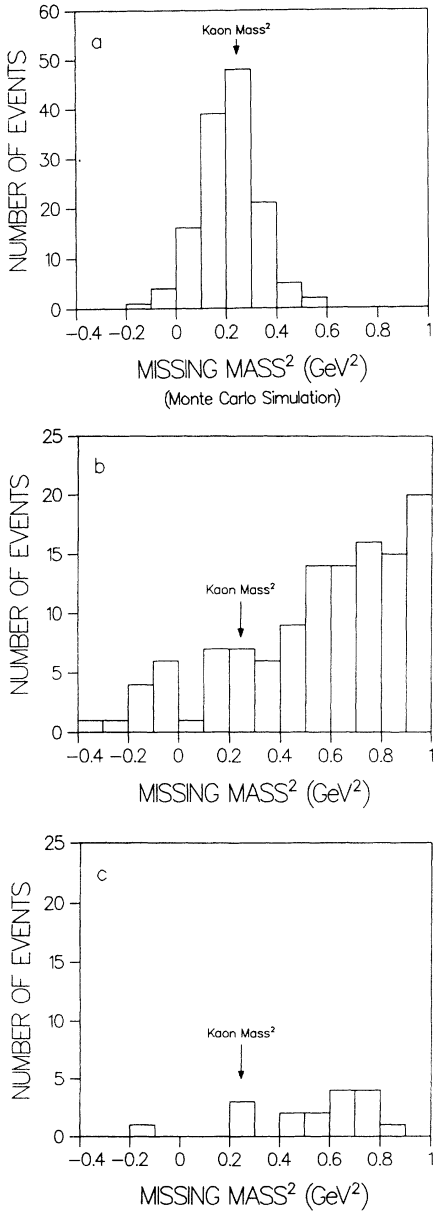

FIG. 20. Missing mass squared for $\pi^-p \rightarrow \Lambda X$. The K^0 peak for $\pi^-p \rightarrow \Lambda K^0$ was expected to be between -0.1 and -0.5 GeV^2 according to the Monte Carlo simulation shown in (a). (b) shows missing mass squared for all Λ's and is background dominated. (c) shows missing mass squared for Λ's in exclusive events for $-5.3 < t < -4.5$ (GeV/c)^2.

TABLE IV. Cross sections at 90 degrees and 5.9 GeV/c incident beam momentum. Reaction number refers to Fig. 27. The values represent interpolations where the range spans 90°.

Number	Reaction	Cross section [nb/(GeV/c)^2]
1	$\pi^+ p \to p\pi^+$	132 ± 10
2	$\pi^- p \to p\pi^-$	73 ± 5
3	$K^+ p \to pK^+$	219 ± 30
4	$K^- p \to pK^-$	18 ± 6
5	$\pi^+ p \to p\rho^+$	214 ± 30
6	$\pi^- p \to p\rho^-$	99 ± 13
7	$K^+ p \to pK^{*+}$	$291 + 47 - 130$
8	$K^- p \to pK^{*-}$	$15 + 10 - 13$
9	$K^- p \to \pi^- \Sigma^+$	50 ± 21
10	$K^- p \to \pi^+ \Sigma^-$	4 ± 3
11	$K^- p \to \Lambda\pi^0$	< 80
12	$\pi^- p \to \Lambda K^0$	< 5
13	$\pi^+ p \to \pi^+ \Delta^+$	45 ± 10
14	$\pi^- p \to \pi^- \Delta^+$	20 ± 11
15	$\pi^- p \to \pi^+ \Delta^-$	24 ± 5
16	$K^+ p \to K^+ \Delta^+$	< 230
17	$pp \to pp$	3300 ± 40
18	$\bar{p}p \to p\bar{p}$	75 ± 8
19	$\bar{p}p \to \pi^+ \pi^-$	7 ± 3
20	$\bar{p}p \to K^+ K^-$	2 ± 2

events in this region, consistent with background. There were no K^- beam events within the π^0 missing mass squared region.

The upper limit we obtained for the cross section for $\pi^- p \to \Lambda K^0$ was based on the observation of 5 events with a background of 5 events. For a Poisson distribution, the number of events for a 90% confidence limit is 5.0 events. This gives an upper limit for t between -5.3 and -4.5 (GeV/c)^2 of 5 nb/(GeV/c)^2. The upper limit for $K^- p \to \Lambda\pi^0$ was based on the 90% confidence level of 2.3 events for a Poisson distribution if no events are seen. The upper limit for this reaction was 80 nb/(GeV/c)^2 for t between -5.5 to -4.8 (GeV/c)^2.

All the cross sections are given in the Appendix, along with an example calculation. The systematic errors shown in the Appendix include an uncertainty in beam normalization (10%), obtained by comparing different monitors, and an estimate of the error in determining the acceptance, which depends on the particular reaction. The beam momentum is uncertain to 1%. Because of the strong energy dependence of these cross sections, this uncertainty introduces 8% overall normalization error when comparing results from different experiments. In Table IV we give the cross-section values at 90° c.m.

DISCUSSION AND CONCLUSIONS

In this section we discuss the results and present conclusions from this experimental program. Numerical values for the cross sections are presented in the Appendix. First we present the angular dependence for five of the cross sections near 90° c.m. Next, we compare the 5.9 GeV/c data presented here to our previous 9.9 GeV/c data, testing scaling both for elastics and quasielastic reactions. Finally, our major goal has been to study the dynamics of large angle exclusive scattering. We present the results for a large number of reactions near 90° c.m. By comparing different reactions, we can study the relative importance of different reaction mechanisms.

Angular distributions and comparison to other experiments

In this section we present the angular distributions for the reactions for which there are a sufficient number of events for more than one bin. These include the three elastic reactions, pp, $\pi^\pm p$, and ρ production: $\pi^\pm p \to \rho^\pm p$. We also take this opportunity to compare to data from some other elastic experiments in the same kinematic region.

In Fig. 21 we display the pp elastic data from this experiment. In addition to the statistical errors shown in the plot, there is an overall normalization error of 13%. Since the pp elastic cross section is symmetric about $\theta_{\text{c.m.}} = 90°$, we have overlapping points from protons which enter the spectrometer arm forward and backward of $\theta_{\text{c.m.}} = 90°$. The agreement within statistical errors between the two sets of cross sections indicates that the detection efficiency is symmetric to better than 4%. The curve drawn through the data is of the form, $a + c[t - t(90°)]^2$. The probability of this fit is less than 1%, indicating that another structure or some residual systematic effect might be present.

In Fig. 22 we plot again our pp elastic data along with the angular distribution of Jenkins *et al.* [10] and the $\theta_{\text{c.m.}} = 90°$ point of Akerlof *et al.* [21]. The beam momenta of both of these experiments was 5.9 GeV/c. When the stated systematic errors of 13, 10, and 9% are included, the three experiments are in good agreement.

The $\pi^- p$ elastic cross section is displayed in Fig. 23.

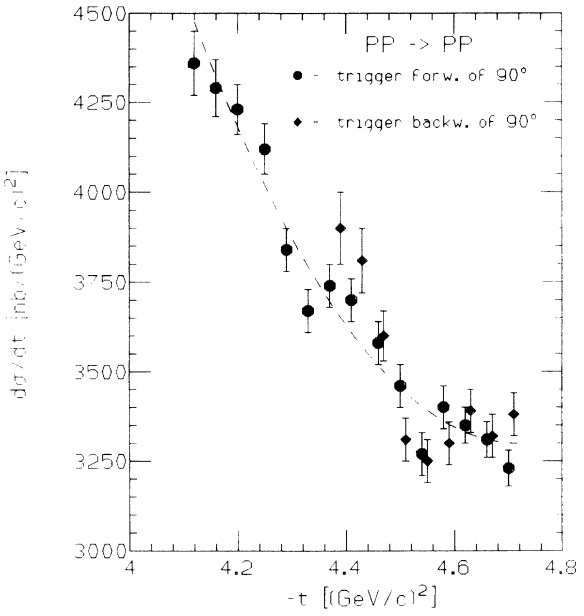

FIG. 21. The differential cross section for *pp* elastic scattering. Data points are included for events with the spectrometer particle forward or backward of the symmetric 90° point. The fitted curve is described in the text.

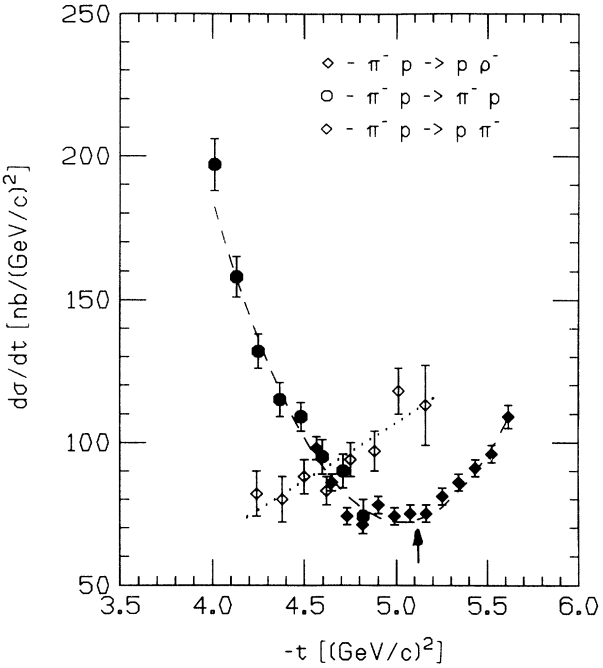

FIG. 23. The differential cross sections are plotted for the reactions $\pi^- p$ elastic and $\pi^- p \to p\rho^-$. The arrow shows the 90° point for $\pi^- p$ elastic scattering. The corresponding point for ρ production is 4.81 $(\mathrm{GeV}/c)^2$.

There are events for which the π^- is in the magnetic spectrometer, and events with the proton in the spectrometer. There is good agreement between the two data sets. The cross section shows a minimum very near the momentum transfer corresponding to $\theta_{\mathrm{c.m.}} = 90°$. A quadratic fit to the data also indicates this well defined minimum.

The reaction $\pi^- p \to \rho^- p$ has a considerably different behavior. The cross section shows a steady rise with momentum transfer (or is flat) in this angular range, as shown in Fig. 23.

There are two other data sets for $\pi^- p$ elastic scattering at an incident momentum of 5.9 GeV/c as shown in Fig. 24. Within the normalization errors, both experi-

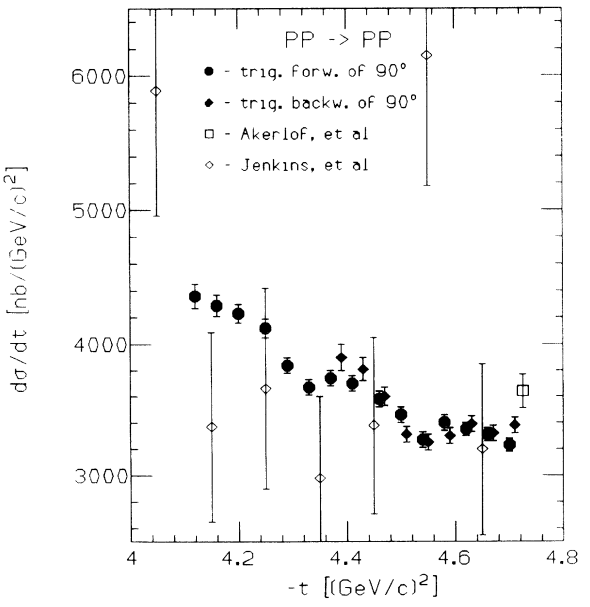

FIG. 22. The results of Jenkins *et al.* [10] and Akerlof *et al.* [21] for *pp* elastic scattering are compared to the results from this experiment.

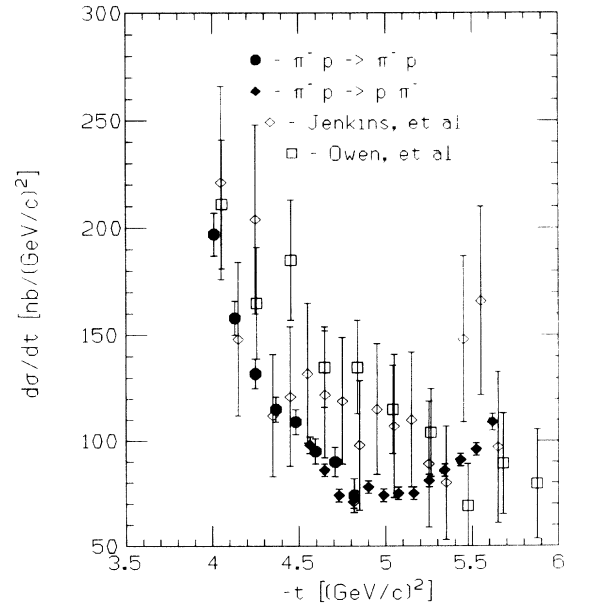

FIG. 24. Results from this experiment on $\pi^- p$ elastic scattering are compared to Owen *et al.* [22] and Jenkins *et al.* [10]. All of these experiments had an incident momentum of 5.9 GeV/c.

ments are in agreement with ours. The measurements of Jenkins *et al.* show the same minimum as this experiment. The cross sections of Owen *et al.* [22], however, fall monotonically with increasing momentum transfer.

The shape of the π^+p elastic differential cross section is very similar to that of the π^-p elastics as shown in Fig. 25. The minimum is slightly lower (0.2) in momentum transfer. Within the statistical errors, the differential cross sections measured by Jenkins *et al.* [10] at the same momentum are in agreement.

The ρ^+ production reaction is consistent with a flat distribution considerably larger than the π^+p minimum, as shown in Fig. 25.

Scaling. Most models of exclusive reactions at large momentum transfers predict a definite scaling behavior. That is, at a fixed c.m. angle, the cross section should fall like a power of s. For PQCD, the power is -8 for meson-baryon reactions and -10 for baryon-baryon reactions. For pp and πp elastic scattering, these PQCD scaling relations are nearly satisfied for incident momenta above 5 GeV/c, but there are oscillations of up to a factor of 2 about the scaling curve [23].

The results from E755 at 9.9 GeV/c can be compared to the results of this experiment at 5.9 GeV/c to determine the energy dependence for eight meson-baryon and two baryon-baryon exclusive reactions. The same apparatus was used for both E755 and E838 so that when comparing ratios the systematic errors are minimized.

In order to satisfy the scaling relation exactly, the center-of-mass angle must be fixed between the two data sets. Whenever possible, the data points used for scaling were taken at 90° c.m. However, the variation of the cross sections about 90° is small, such that the small variations in $\theta_{\text{c.m.}}$ between the experiments produced systematic errors smaller than the statistical errors.

The results are tabulated in Table V and plotted in Fig. 26. While the ratios of the reactions do not agree perfectly with the expected scaling relation, they are all within one power of s except for reaction 15. The overall pattern as shown in Fig. 26 is remarkably consistent. This level of consistency is about what is expected at these moderately low momenta. Reaction 15 shows other anomalies as explained elsewhere in the text.

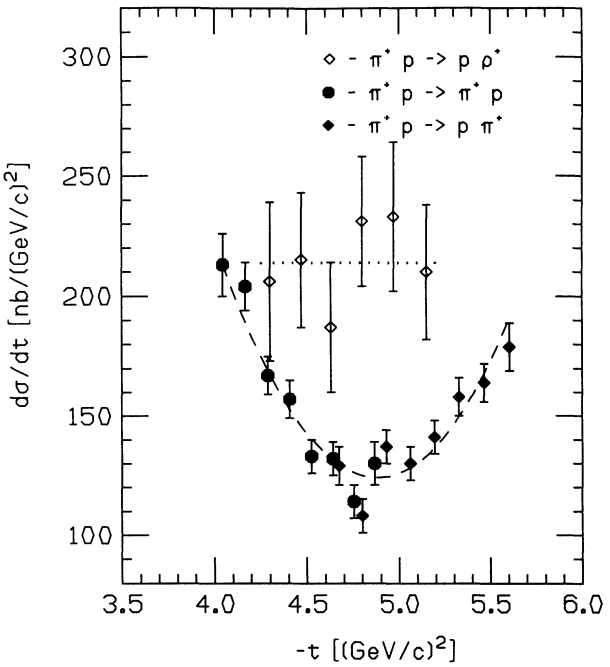

FIG. 25. The differential cross sections for π^+p elastic scattering and the reaction $\pi^+p \to p\rho^+$ are plotted. The fitted curves are discussed in the text.

We conclude that the scaling relations for all reactions except $\pi^-p \to \pi^+\Delta^-$, are as good as those seen in pp and π^-p elastic scattering. This indicates that nearly all exclusive reactions have entered a scaling region by 5.9 GeV/c.

We have also compared the Λ results with lower energy data, using s^{-8} scaling, although the lower energy results are not in the scaling region. Loverre *et al.* [18] measured $\pi^-p \to \Lambda K^0$ at 3.95 GeV/c and Bachman *et al.* [19] at 3.15 GeV/c, both at 90° c.m. The Loverre result scales to 22±7 nb/(GeV/c)^2 and the Bachman result scales to 19±8 nb/(GeV/c)^2; our upper limit is 5 nb/(GeV/c)^2. Marzano *et al.* [20] measured $K^-p \to \Lambda\pi^0$ at 4.2 GeV/c, 90° c.m., and their result scales to 76±18 nb/(GeV/c)^2, compared with our upper limit of 80 nb/(GeV/c)^2.

TABLE V. The scaling between E755 and E838 has been measured for eight meson-baryon and 2 baryon-baryon interactions at $\theta_{\text{c.m.}} = 90°$. The nominal beam momentum was 5.9 GeV/c and 9.9 GeV/c for E838 and E755, respectively. There is also an overall systematic error of $\Delta n_{\text{syst}} = \pm 0.3$ from systematic errors of ±13% for E838 and ±9% for E755.

		Cross section		n-2
No.	Interaction	E838	E755	$(\frac{d\sigma}{dt} \sim 1/s^{n-2})$
1	$\pi^+p \to p\pi^+$	132 ± 10	4.6 ± 0.3	6.7 ± 0.2
2	$\pi^-p \to p\pi^-$	73 ± 5	1.7 ± 0.2	7.5 ± 0.3
3	$K^+p \to pK^+$	219 ± 30	3.4 ± 1.4	$8.3^{+0.6}_{-1.0}$
4	$K^-p \to pK^-$	18 ± 6	0.9 ± 0.9	≥ 3.9
5	$\pi^+p \to p\rho^+$	214 ± 30	3.4 ± 0.7	8.3 ± 0.5
6	$\pi^-p \to p\rho^-$	99 ± 13	1.3 ± 0.6	8.7 ± 1.0
13	$\pi^+p \to \pi^+\Delta^+$	45 ± 10	2.0 ± 0.6	6.2 ± 0.8
15	$\pi^-p \to \pi^+\Delta^-$	24 ± 5	≤ 0.12	≥ 10.1
17	$pp \to pp$	3300 ± 40	48 ± 5	9.1 ± 0.2
18	$\bar{p}p \to p\bar{p}$	75 ± 8	≤ 2.1	≥ 7.5

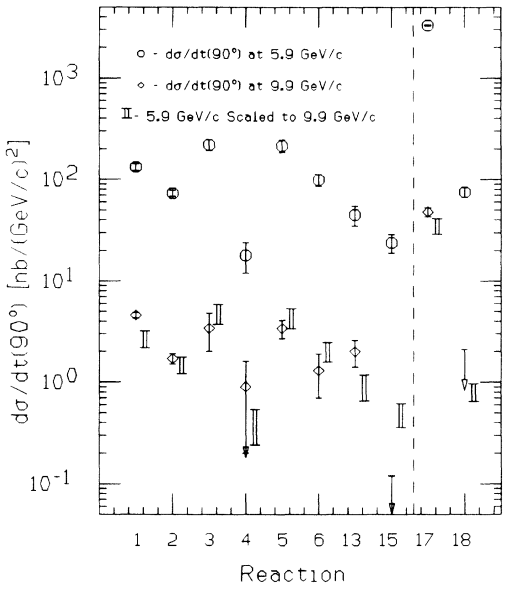

FIG. 26. The scaling between E755 and E838 has been calculated for eight meson-baryon and 2 baryon-baryon interactions at $\theta_{c.m.} = 90°$. The beam momentum for E838 was 5.9 GeV/c, corresponding to $s = 11.9$ GeV^2 for meson-baryon reactions and $s = 12.9$ GeV^2 for baryon-baryon reactions. For the 9.9 GeV/c momentum of E755, the corresponding values of s are 19.6 and 20.5 GeV^2.

Reaction mechanisms. Several striking features are seen in the variations among the 20 exclusive cross sections measured in this experiment. The magnitudes of the 90° cross sections are displayed in Fig. 27 (and Table IV). These show differences of up to 2 orders of magnitude. In comparison, the total cross sections between particle and antiparticle are nearly the same, and the overall variation in the total cross section between pion, kaon, and proton is less than a factor of 3. This 90° result indicates that very different dynamical processes are important at high momentum transfer.

We will compare our measured cross sections, based on the broad classes of quark amplitudes developed for exclusives. The formalism assumes, following the observed scaling of fixed angle cross sections and dimensional counting arguments, that only valence quarks participate in the large angle exclusive scattering. Four general classes of reaction mechanisms have been introduced, involving the flow of valence quarks in the interaction, as shown in Fig. 1. The classes of amplitudes that contribute to each reaction we have measured are indicated in Fig. 27.

Generally, one can see in Fig. 27 that the reactions that involve quark interchange have larger cross sections. We can also see that gluon exchange contributions are small. This was noted in our previous experiment E755, and these new results strongly support this conclusion.

If we compare the $\bar{p}p$ and pp elastic cross sections, we would expect similar cross sections if gluon exchange were dominant. On the other hand, quark interchange cannot contribute to $\bar{p}p$ elastics, since the p and $\bar{p}$ do not have any valence quarks in common. We have measured the 90° c.m. $\bar{p}p$ cross section in the scaling region for the first time (we placed an upper limit on it in E755), and we observe the ratio $R(\bar{p}p/pp) = 0.023 \pm 0.002$ at 90° c.m. At 0° the ratio is approximately 1.7 at 6 GeV/c.

A second pair of reactions which are sensitive to this comparison is $K^{\pm}p$ elastic scattering. The valence quarks in the K^+ are $(u\bar{s})$, and quark interchange is possible between the K^+ and proton. The K^- and proton have no valence quarks in common and quark interchange cannot contribute. We observe $R(K^-p/K^+p) = 0.08 \pm 0.03$, supporting quark interchange dominance. This ratio was poorly measured in E755.

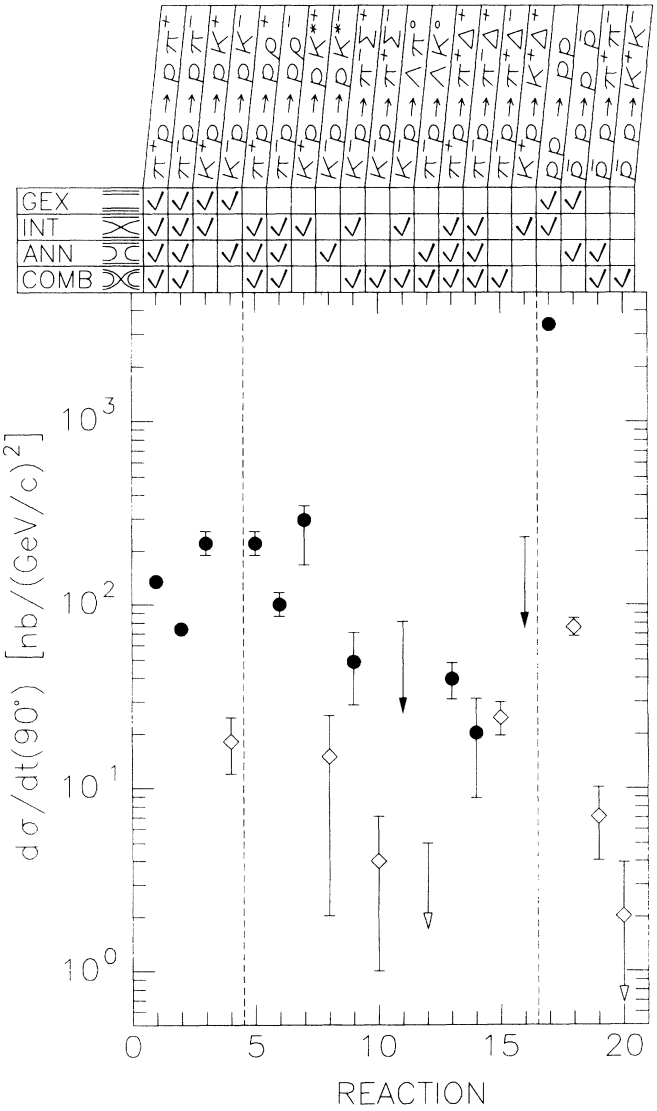

FIG. 27. Differential cross sections for the 16 meson-baryon and 4 baryon-baryon measured in this experiment. The cross sections are at, or extrapolated from, near 90° center of mass. The four quark flow diagrams which contribute to each of the 20 reactions are given in the chart at the top of the figure. Those reactions which have a contribution from quark interchange(INT) are given by the solid black points. As can be seen, these are the largest cross sections.

The reactions $K^{\pm}p \to K^{*\pm}p$ can also be used to compare quark interchange with annihilation. The K^+p reaction may proceed via quark interchange, and K^-p via only annihilation. Gluon exchange cannot contribute to either reaction. We observe $R(K^-p \to K^{*-}p/K^+p \to K^{*+}p) = 0.05 \pm 0.04$. These are the first measurements of these reactions in the scaling region.

For the Σ reactions, an s-quark interchange can mediate $K^-p \to \pi^-\Sigma^-$, and only a combination of interchange and annihilation contribute to $K^-p \to \pi^+\Sigma^-$. We observe the ratio $R(K^-p \to \pi^+\Sigma^-/K^-p \to \pi^-\Sigma^+) = 0.08 \pm 0.07$. This is also the first measurement of these reactions in the scaling region.

The $\bar{p}p \to \pi^+\pi^-$ and $\to K^+K^-$ reactions can be compared to π^+p and K^+p elastic reactions, respectively. Quark interchange cannot contribute to the $\bar{p}p$ reactions. We observe $R(\bar{p}p \to \pi^+\pi^-/\pi^+p \to \pi^+p) = 0.05 \pm 0.02$ and $R(\bar{p}p \to K^+K^-/K^+p \to K^+p) = 0.01 \pm 0.01$. Again, these reaction cross sections agree well with quark interchange dominance.

It is interesting to compare the $\pi p \to \pi\Delta$ reactions. The reaction $\pi^-p \to \pi^+\Delta^-$ has only a combined quark interchange and annihilation contribution. The observed cross section is small, similar to K^-p elastics and $K^-p \to K^{*-}p$ which do not have a quark interchange contribution. However, the reactions $\pi^+p \to \pi^+\Delta^+$ and $\pi^-p \to \pi^-\Delta^+$ have allowed quark interchange contributions, and both cross sections are also small. If we confine ourselves to quark interchange amplitudes, and assume that the two chirality amplitudes for quark interchange are the same sign and size (this can be deduced from the π^+p/π^-p elastic ratio, if quark interchange is dominant), the chirality amplitudes partially cancel in the case of $\pi^+p \to \pi^+\Delta^+$, and completely cancel for $\pi^-p \to \pi^-\Delta^+$. These cancellations result from the Δ^+ SU(6) wave function. We observe $R(\pi^+p \to \pi^+\Delta^+/\pi^-p \to \pi^+\Delta^-) = 1.9 \pm 0.6$ and $R(\pi^-p \to \pi^-\Delta^+/\pi^-p \to \pi^+\Delta^-) = 0.8 \pm 0.5$. These are in good qualitative agreement with dominance of quark interchange. These reactions have not been measured before in the scaling region.

For the Λ reactions, the measured upper limits do not contradict dominance of quark interchange. The $K^-p \to \Lambda\pi^0$ reaction, which may proceed by s-quark interchange, has an upper limit comparable to $K^-p \to \pi^-\Sigma^+$ where s-quark interchange is also allowed. The $\pi^-p \to \Lambda K^0$ reaction has annihilation and combination (quark interchange and annihilation, Fig. 1) amplitudes. The upper limit for this reaction is comparable to the measured $K^-p \to \pi^+\Sigma^-$ cross section, which has only combination amplitudes.

One can, in addition to these comparisons, attempt to test Farrar's expansion of the scattering amplitudes into valence quark scattering amplitudes. This can be done to a certain extent (see theses by C. White and R. Appel), but normalization between meson wave functions is required, and the result is inconclusive.

Another regularity in the cross sections which is evident from Fig. 27 is that vector meson production at 90° is generally larger than the corresponding elastic reaction by about 30%: $(\pi^+p \to p\rho^+)/(\pi^+p \text{ elastic}) = 1.6 \pm 0.3$, $(\pi^-p \to p\rho^-)/(\pi^-p \text{ elastic}) = 1.4 \pm 0.2$, $(K^+p \to pK^{*+})/(K^+p \text{ elastic}) = 1.3^{+0.3}_{-0.6}$, and $(K^-p \to pK^{*-})/(K^-p \text{ elastic}) = 0.8^{+0.6}_{-0.8}$. We also remark that 90° Δ production, when compared to elastics, has similar ratios for the two charge signs: $(\pi^+p \to \pi^+\Delta^+)/(\pi^+p \text{ elastic}) = 0.34 \pm 0.08$ and $(\pi^-p \to \pi^-\Delta^+)/(\pi^-p \text{ elastic}) = 0.27 \pm 0.15$.

The present results appear to support the approach involving classes of valence quark scattering amplitudes, in that a simple mechanism, the dominance of quark interchange, gives a consistent picture over a large number of exclusive reactions. The applicability of PQCD or of another model would be much clearer if and when predictions of cross sections and the relative strength of quark interchange diagrams become available.

SUMMARY

In summary, we have measured a large number of exclusive reactions of varying charge, flavor, and spin for an incident momentum of 5.9 GeV/c. These reactions allow a rather detailed study of quark flow in high momentum transfer interactions (something which is difficult to do in inclusive reactions). The applicability of perturbative QCD for 90° exclusive reactions has not been firmly established in the 6 to 10 GeV/c region. Considering the relatively low energy of these experiments, the data show a surprising consistency with the PQCD approach. The dominance of valance quark scattering is indicated by the agreement with the dimensional scaling for all but one of the reactions studied. Previous color transparency measurements (BNL E834) give strong evidence for the minihadrons implied by the PQCD approach. Future experiments with the EVA detector (BNL E850) will study this phenomenon in more detail and at higher momenta. The most striking feature of this data, which had been previously noted at 10 GeV/c, is the dominance of the reactions with quark interchange. This enables us to predict which cross sections will be large, and should lead to a rather simple picture when more complete calculations have been done.

ACKNOWLEDGMENTS

Experiment E838 was the last in a series of experiments designed to study exclusive reactions with a dedicated detector at the AGS. We would like to express special thanks to the members of E755 who helped build this versatile apparatus: B. R. Baller, G. C. Blazey, E. A. Petersen, and D. S. Wahl. We wish to thank all the members of the AGS Department who contributed to the successful completion of this experiment. D. Dayton was our liason engineer who quickly and efficiently responded to our requests for services. The EAG Group headed by A. Pendzick supplied all of our necessary services, and maintained the C1 beam line. The Cryo Group under R. Meier carefully maintained our liquid hydrogen target. The fine beam particle identification needed to study these reactions was based on the two differential Cherenkov counters supplied by T. F. Kycia of the BNL Physics Department. His technical staff helped install

and maintain these counters. We wish to acknowledge useful discussions with many people: S. Brodsky, G. Farrar, N. Isgur, A. Mueller, J. Ralston, J. Soffer, and G. Sterman. Inspiration for this series of experiments came from a talk given by P. Grannis in a 1979 AGS workshop. P. Nemethy guided the thesis research of R.A. This work was performed under the auspices of the U.S. Department of Energy and the National Science Foundation.

APPENDIX A

In this appendix we list the numerical values for the 20 different differential cross sections measured in this experiment.

The measurement of the differential cross section can be expressed by the following equation:

$$\frac{d\sigma}{dt} = \left(\frac{\text{No. of events}}{\text{Beam Flux}}\right) \frac{1}{(\rho_{H_2} l)/m_H} \frac{1}{V_{acc}\Delta t} \times \text{corrections} . \tag{A1}$$

The first term represents the number of observed events divided by the total number of beam particles on target. The second term, constant for all reactions, determines the density of scattering centers per unit area for the target, where ρ_{H_2} is the density of liquid hydrogen, l equals the length of the target, and m_H is the mass of the hydrogen atom.

$$\rho_{H_2} = .0708\ \text{g/cm}^3,\ l = 99.0\ \text{cm},\ \text{and}\ m_H = 1.673 \times 10^{-24}\ \text{g}$$

so

$$[(\rho_{H_2} \cdot l)/m_H] = 4.19 \times 10^{24}\ \text{cm}^{-2} = 4.19\ \text{barns}^{-1}$$

V_{acc} refers to the acceptance value determined by the Monte Carlo, and Δt equals the size of the t bin. The correction terms include selection and identification efficiencies, loss due to absorption of final-state particles in the apparatus, and hardware efficiencies. As an example, we have listed the terms used in the calculation of the differential cross section for the interaction $\pi^+ p \to \rho^+ p$:

Event parameters:

P_B	5.89 ± 0.05 GeV/c
S	11.96 (GeV/c)^2
W	3.46 (GeV/c)^2

Pions on target	$1.09 \times 10^{12} \pm 0.07 \times 10^{12}$
Experimental range	$-0.12 \leq \cos(\theta_{c.m.}) \leq .09$
$t_{\theta_{c.m.}=\pi/2}$	4.78 (GeV/c)^2

Corrections:

Absorption	Hardware	Recon	Kin. cuts	π_b ID Eff.	π_{sp} ID Eff.
1.14 ± 0.03	1.15 ± 0.03	1.19 ± 0.03	1.43 ± 0.06	1.41 ± 0.02	1.04 ± 0.01

Experimental numbers:

Scat. angle	t (momentum transfer)	Acceptance	$d\sigma/dt$
24.5-25.3	-5.15 ± 0.18 (GeV/c)^2	0.0139 ± 0.0008	210 ± 10 nb
25.3-26.1	-4.97 ± 0.17	0.0198 ± .0009	233 ± 10
26.1-26.9	-4.80 ± 0.17	0.0231 ± 0.0011	231 ± 10
26.9-27.7	-4.63 ± 0.17	0.0231 ± 0.0010	187 ± 10
27.7-28.5	-4.47 ± 0.16	0.0201 ± 0.0008	215 ± 10
28.5-29.3	-4.30 ± 0.16	0.0135 ± 0.0008	206 ± 10

The measured cross sections follow, with the reaction number used in the text indicated. All of these cross sections are quoted at an incident momentum of 5.9 GeV/c. Whenever there are sufficient events, we have given the values for several bins near 90° in the center of mass. The four-momentum transfer squared, t, is defined in the standard way. For meson-baryon reactions, it is the difference of the final state and initial state meson momenta. For pp elastics, t is defined only for scattering angles < 90°. For $\bar{p}p$ reactions, t is the difference between the final and initial state $\bar{p}$ momenta for elastics, and is the difference between the negatively charged final state meson and the initial $\bar{p}$ momenta for $\bar{p}p \to \pi^+\pi^-$ and $\bar{p}p \to K^+K^-$. For the pp and πp elastic scattering data there are overlapping sets

of data depending on which particle is measured in the spectrometer. The error on the momentum transfer reflects the size of the bin, not its uncertainty. The error on the number of events is either its statistical error for elastic reactions or fitting error for inelastic reactions. Both the statistical and individual systematic errors are given for the differential cross sections. All differential cross sections are listed in nanobarns/(GeV/c)^2.

1: $\pi^+ + p \to p + \pi^+$

$-t$ (GeV/c)^2	No. events	$d\sigma/dt$	$-t$ (GeV/c)^2	No. events	$d\sigma/dt$
4.045 ± 0.123	413 ± 25	213 ± 13 ± 28	4.800 ± 0.127	415 ± 25	108 ± 7 ± 14
4.168 ± 0.121	605 ± 30	204 ± 10 ± 27	4.865 ± 0.110	290 ± 20	130 ± 9 ± 10
4.288 ± 0.119	575 ± 25	167 ± 8 ± 17	4.929 ± 0.129	603 ± 30	137 ± 7 ± 18
4.407 ± 0.117	624 ± 30	157 ± 8 ± 15	5.060 ± 0.131	620 ± 30	130 ± 7 ± 17
4.524 ± 0.115	525 ± 25	133 ± 7 ± 14	5.193 ± 0.133	672 ± 30	141 ± 7 ± 18
4.640 ± 0.113	480 ± 25	132 ± 7 ± 12	5.328 ± 0.135	650 ± 30	158 ± 8 ± 21
4.673 ± 0.127	353 ± 20	129 ± 8 ± 17	5.466 ± 0.137	565 ± 25	164 ± 8 ± 21
4.753 ± 0.112	361 ± 20	114 ± 7 ± 12	5.605 ± 0.138	380 ± 20	179 ± 10 ± 23

2: $\pi^- + p \to p + \pi^-$

$-t$ (GeV/c)^2	No. events	$d\sigma/dt$	$-t$ (GeV/c)^2	No. events	$d\sigma/dt$
4.010 ± 0.120	590 ± 25	197 ± 9 ±26	4.819 ± 0.108	195 ± 15	74 ± 6 ± 10
4.130 ± 0.119	687 ± 30	158 ± 7 ± 21	4.901 ± 0.086	1640 ± 45	78 ± 3 ± 10
4.249 ± 0.118	660 ± 30	132 ± 6 ± 17	4.988 ± 0.087	1640 ± 45	74 ± 3 ± 10
4.367 ± 0.116	620 ± 30	115 ± 6 ± 15	5.075 ± 0.087	1699 ± 45	75 ± 3 ± 10
4.482 ± 0.114	575 ± 25	109 ± 5 ±14	5.163 ± 0.088	1715 ± 45	75 ± 3 ± 10
4.565 ± 0.083	790 ± 30	98 ± 4 ± 13	5.252 ± 0.089	1680 ± 45	81 ± 3 ± 11
4.596 ± 0.112	460 ± 25	95 ± 6 ± 12	5.342 ± 0.090	1670 ± 45	86 ± 3 ± 11
4.648 ± 0.083	1100± 35	86 ± 3 ± 11	5.433 ± 0.091	1580 ± 45	91 ± 3 ± 12
4.709 ± 0.110	357 ± 20	90 ± 6 ± 12	5.524 ± 0.091	1250 ± 40	96 ± 3 ± 12
4.731 ± 0.084	1250± 40	74 ± 3 ± 10	5.617 ± 0.092	906 ± 35	109 ± 4 ± 14
4.816 ± 0.085	1360± 40	71 ± 3 ± 9			

3: $K^+ + p \to p + K^+$			4: $K^- + p \to p + K^-$		
$-t$ (GeV/c)^2	No. events	$d\sigma/dt$	$-t$ (GeV/c)^2	No. events	$d\sigma/dt$
4.76 ± 0.48	80 ± 10	219 ± 27 ± 28	5.03 ± 1.04	22 ± 7	18 ± 6 ± 2

5: $\pi^+ + p \to p + \rho^+$			6: $\pi^- + p \to p + \rho^-$		
$-t$ (GeV/c)^2	No. events	$d\sigma/dt$	$-t$ (GeV/c)^2	No. events	$d\sigma/dt$
−5.15 ± 0.18	740 ± 100	210 ± 28± 29	−5.16 ± 0.15	2475± 300	113 ± 14 ± 16
−4.97 ± 0.17	1140± 150	233 ± 31± 29	−5.01 ± 0.13	3050± 200	118 ± 8 ± 15
−4.80 ± 0.17	1295± 150	231 ± 27± 28	−4.88 ± 0.13	2875± 200	97 ± 7 ± 12
−4.63 ± 0.17	1025± 150	187 ± 27± 22	−4.75 ± 0.13	2950± 175	94 ± 6 ± 11
−4.47 ± 0.16	1000± 130	215 ± 28± 28	−4.62 ± 0.12	2630± 150	83 ± 5 ± 10
−4.30 ± 0.16	630 ± 100	206 ± 33± 29	−4.50 ± 0.12	2450± 150	88 ± 6 ± 11
			−4.38 ± 0.12	1900± 175	80 ± 8 ± 10
			−4.24 ± 0.14	1525± 150	82 ± 8 ± 11

7: $K^+ + p \to p + K^{*+}$			8: $K^- + p \to p + K^{*-}$		
$-t$ (GeV/c)^2	No. events	$d\sigma/dt$	$-t$ (GeV/c)^2	No. events	$d\sigma/dt$
−4.69 ± 1.20	154^{+25}_{-62}	291^{+47}_{-130}± 44	−4.66 ± 1.19	35^{+15}_{-20}	15^{+7}_{-9} ± 2

9: $K^- + p \to \pi^- + \Sigma^+$			10: $K^- + p \to \pi^+ + \Sigma^-$		
$-t$ (GeV/c)^2	No. events	$d\sigma/dt$	$-t$ (GeV/c)^2	No. events	$d\sigma/dt$
−4.15 ± 0.95	8 ± 3	57 ± 21 ± 10	−4.15 ± 0.95	4 ± 3	4 ± 3 ± 1

11: $K^- + p \to \Lambda + \pi^0$			12: $\pi^- + p \to \Lambda + K^0$		
$-t$ (GeV/c)^2	No. events	$d\sigma/dt$	$-t$ (GeV/c)^2	No. events	$d\sigma/dt$
−5.15 ± 0.35	2.3	< 80 90%	−4.9 ± 0.4	5.0	< 5 90%

13: $\pi^+ + p \to \pi^+ + \Delta^+$			15: $\pi^- + p \to \pi^+ + \Delta^-$		
$-t$ (GeV/c)^2	No. events	$d\sigma/dt$	$-t$ (GeV/c)^2	No. events	$d\sigma/dt$
−4.20 ± 1.06	1500^{+310}_{-220}	51^{+11}_{-8} ± 7	−3.84 ± 0.23	1420±120	28 ± 3 ± 4
14: $\pi^- + p \to \pi^- + \Delta^+$			−4.06 ± 0.22	1890±140	30 ± 3 ± 4
$-t$ (GeV/c)^2	No. events	$d\sigma/dt$	−4.28 ± 0.21	1510±130	25 ± 3 ± 3
−4.15 ± 1.05	1000^{+300}_{-400}	23^{+7}_{-9} ± 3	−4.49 ± 0.21	990±120	25 ± 3 ± 3

16: $K^+ + p \to K^+ + \Delta^+$

$-t$ (GeV/c)^2	No. events	$d\sigma/dt$
-4.24 ± 1.08	<60	< 230 90%

17: $p + p \to p + p$

$-t$ (GeV/c)^2	No. events	$d\sigma/dt$	$-t$ (GeV/c)^2	No. events	$d\sigma/dt$
4.12 ± 0.043	2905 ± 60	$4360 \pm 90 \pm 480$	4.62 ± 0.041	4560 ± 70	$3350 \pm 50 \pm 370$
4.16 ± 0.043	3470 ± 65	$4290 \pm 80 \pm 470$	4.66 ± 0.041	4545 ± 70	$3310 \pm 50 \pm 360$
4.20 ± 0.043	4080 ± 65	$4230 \pm 70 \pm 470$	4.70 ± 0.041	4375 ± 70	$3230 \pm 50 \pm 360$
4.25 ± 0.042	4380 ± 70	$4120 \pm 65 \pm 450$	4.71 ± 0.040	4300 ± 70	$3380 \pm 55 \pm 370$
4.29 ± 0.042	4440 ± 70	$3840 \pm 60 \pm 420$	4.67 ± 0.040	4179 ± 70	$3320 \pm 55 \pm 370$
4.33 ± 0.042	4460 ± 70	$3670 \pm 60 \pm 400$	4.63 ± 0.040	3860 ± 65	$3390 \pm 60 \pm 370$
4.37 ± 0.042	4590 ± 70	$3740 \pm 60 \pm 410$	4.59 ± 0.040	3585 ± 65	$3300 \pm 60 \pm 360$
4.41 ± 0.042	4783 ± 75	$3700 \pm 60 \pm 410$	4.55 ± 0.039	3340 ± 60	$3250 \pm 60 \pm 360$
4.46 ± 0.042	4700 ± 75	$3580 \pm 60 \pm 390$	4.51 ± 0.039	3075 ± 60	$3310 \pm 65 \pm 360$
4.50 ± 0.041	4830 ± 75	$3460 \pm 55 \pm 380$	4.47 ± 0.039	2965 ± 60	$3600 \pm 75 \pm 400$
4.54 ± 0.041	4569 ± 70	$3270 \pm 50 \pm 360$	4.43 ± 0.039	2625 ± 55	$3810 \pm 80 \pm 420$
4.58 ± 0.041	4760 ± 75	$3400 \pm 55 \pm 370$	4.39 ± 0.039	2115 ± 50	$3900 \pm 95 \pm 430$

18: $\bar{p} + p \to p + \bar{p}$

$-t$ (GeV/c)^2	No. events	$d\sigma/dt$
4.82 ± 0.98	123 ± 11	$75 \pm 7 \pm 11$

18: $\bar{p} + p \to \bar{p} + p$

$-t$ (GeV/c)^2	No. events	$d\sigma/dt$
4.54 ± 0.98	25 ± 5	$87 \pm 18 \pm 12$

19: $\bar{p}p \to \pi^+\pi^-$

$-t$ (GeV/c)^2	No. events	$d\sigma/dt$
6.42 ± 1.00	6 ± 2.4	$7 \pm 3 \pm 1$

20: $\bar{p}p \to K^+K^-$

$-t$ (GeV/c)^2	No. events	$d\sigma/dt$
6.03 ± 0.98	2 ± 1.4	$2 \pm 2 \pm 0.3$

[1] B.R. Baller *et al.*, Phys. Rev. Lett. 60, 1118 (1988); G. C. Blazey *et al.*, *ibid.* **55**, 1820 (1985); (a) This paper is based on C. White, Ph.D. thesis, University of Minnesota, 1990 and on R. Appel, Ph.D. thesis, New York University, 1991.

[2] R. Henzi and P. Valin, Z. Phys. C **27**, 351 (1985).

[3] G. Preparata and N. Craigie, Nucl. Phys. **B102**, 478 (1976); G. Nadulli, G. Preparata, and J. Soffer, Phys. Rev. D **31**, 626 (1985).

[4] J. Szwed, Nucl. Phys. **B229**, 53 (1983).

[5] G. Lepage and S. Brodsky, Phys. Rev. D **22**, 2157 (1980).

[6] A. Mueller, in *Proceedings of the XVII Rencontre de Moriond*, Les Arcs, France, 1982, edited by J. Tran Thanh Van (Editions Frontieres, Gif-sur-Yvette, France, 1982), p. 13; S. J. Brodsky, in *Proceedings of the 13th International Symposium on Multiparticle Dynamics*, edited by W. Kittel, W. Metzger, and A. Stergiou (World Scientific, Singapore, 1982), p. 963.

[7] A. Carroll *et al.*, Phys. Rev. Lett. **61**, 1698 (1988).

[8] V. Matveev, R. Muradyan, and A. Tavhelidze, Lett. Nuovo Cimento **7**, 719 (1973).

[9] S. Brodsky and G. Farrar, Phys. Rev. Lett. **31**, 1153 (1973); Phys. Rev. D **11**, 1309 (1975).

[10] K. Jenkins *et al.*, Phys. Rev. Lett. **40**, 425 (1978).

[11] R. G. Arnold *et al.*, Phys. Rev. Lett. **57**, 174 (1986).

[12] N. Isgur and C.H. Llewellyn Smith, Nucl. Phys. **B317**, 526 (1989).

[13] H-n. Li and G. Sterman, Nucl. Phys. **B381**, 129 (1992).

[14] O. Jacob and L. Kisslinger, Phys. Rev. Lett. **56**, 225 (1986).

[15] D. G. Crabb *et al.*, Phys. Rev. Lett. **64**, 2627 (1990).

[16] S. Heppelmann *et al.*, Phys. Rev. Lett. **55**, 1824 (1985).

[17] G. Farrar, Phys. Rev. Lett. **53**, 28 (1984).

[18] P. F. Loverre *et al.*, Z. Phys. C **6**, 283 (1980).

[19] L. Bachman *et al.*, Nucl. Phys. **B263**, 458 (1986).

[20] F. Marzano *et al.*, Nucl. Phys. **B123**, 203 (1977).

[21] C. Akerlof *et al.*, Phys. Rev. **159**, 1138 (1967).

[22] D. Owen, Phys. Rev. **181**, 1794 (1969).

[23] B. Pire and J. Ralston, Phys. Lett. **117B**, 233 (1982); A. W. Hendry, Phys. Rev. D **10**, 2300 (1974).